

Vortex Design Problem

Bartosz Protas^a

^a*Department of Mathematics & Statistics, McMaster University, Hamilton,
Ontario, Canada*

Abstract

In this investigation we propose a computational approach for solution of optimal control problems for vortex systems with compactly supported vorticity. The problem is formulated as PDE-constrained optimization in which the solutions are found using a gradient-based descent method. Recognizing such Euler flows as free-boundary problems, the proposed approach relies on shape differentiation combined with adjoint analysis to determine cost functional gradients. In explicit tracking of interfaces (vortex boundaries) this method offers an alternative to grid-based techniques, such as the level-set methods, and represents a natural optimization formulation for vortex problems computed using the contour dynamics technique. We develop and validate this approach using the design of 2D equilibrium Euler flows with finite-area vortices as a model problem. It is also discussed how the proposed methodology can be applied to Euler flows featuring other vorticity distributions, such as vortex sheets, and to time-dependent phenomena.

Key words: optimal control, adjoint analysis, vortex flows, free-boundary problems, Prandtl-Batchelor flows

PACS: 47.32.C-, 46.15.Cc, 47.32.Ff

1 Introduction

There is a renewed interest in the computation of inviscid vortex flows featuring vorticity distributions more complicated than point vortices, namely, vortex sheets and vortex patches. Although still mostly limited to two-dimensional (2D) flows, these recent investigations are on the one hand motivated by emerging biomechanical applications where one-dimensional (1D) vortex sheets serve as models of the vortex wake generated by a swimming object, see, e.g., [1, 2, 3, 4, 5, 6]. On the other hand, such studies are inspired

by recent developments in computational complex analysis [7]. In addition, solutions of 2D Euler equations characterized by piecewise constant vorticity continue to find applications in the study of atmospheric and oceanographic phenomena [8, 9]. From the mathematical point of view, a salient feature of all of these models is that they are described by partial differential equations (PDEs) of the free–boundary type in which the shape of the interface (i.e., the vortex sheet, or the boundary of the vortex patch) is a priori unknown and must be determined as a part of the solution of the problem. Computation of such systems is typically based on various versions of the “contour dynamics” approach [10] which has been significantly improved and generalized since its inception. At the same time, over the last decade or so a significant progress has taken place regarding solution of a range of optimization and optimal control problems for fluid systems [11]. Most of approaches proposed relied on solution of suitably–defined adjoint equations to determine the gradient of the cost functional to be minimized, and were usually focused on fixed–boundary problems. While there has been a number of investigations addressing optimization of the shape of the flow domain [12, 13, 14, 15, 16], we are not aware of any results concerning optimization of flow problems with internal interfaces, with the exception of references [17, 18] which however concern a rather different physical problem. Therefore, a long–term objective of the present research effort is to develop an optimization framework suitable for vortex dynamics problems of the type mentioned above. Since solving such optimization problems will typically involve constructing vortex systems with some prescribed properties, we will refer to this broad set of problems as “vortex design”. It should be emphasized, however, that the techniques developed in the present study are applicable to the inviscid case only, as vorticity fields in viscous flows may not have discontinuities. Optimization problems for flows at finite Reynolds numbers are, at least in principle, amenable to solution using standard methods of adjoint–based optimization and we refer the reader to the monograph [11] for a survey and further references.

The problem of controlling and optimizing vortex configurations has already received some attention in the literature, and these efforts were surveyed in a recent review paper [19]. While these earlier investigations were concerned almost exclusively with systems of *point vortices*, here we seek to develop a systematic approach for the optimal control of vortices with more complicated vorticity distributions such as vortex sheets and vortex patches. More specifically, in the present investigation we introduce our approach based on arguably the simplest problem in this class, namely, a steady–state flow with finite–area vortex patches (in fact, dealing with finite–length vortex sheets is technically more complicated due to the presence of the endpoints which act as geometric singularities, and is the subject of ongoing research). A key novelty of our approach is that, recognizing that such systems are in fact described mathematically by equations of the

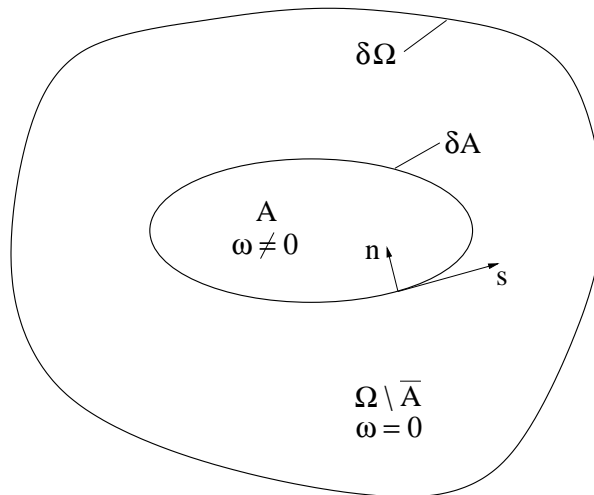


Fig. 1. Schematic illustrating the vortex region A and the flow domain Ω with its boundary $\partial\Omega$. It shows also the orientation of the local coordinate system (s, n) attached to the vortex boundary ∂A .

free-boundary type, our optimization methodology is developed based on methods of the “shape calculus”. The shape calculus is a suite of techniques which allow one to treat PDE problems defined on variable domains and/or involving interfaces [20, 21]. This appears as a natural way to frame an optimization problem for a vortex system, consistent with the “contour dynamics” approach typically employed to solve the “direct” problem of determining the time evolution or the steady states. In this sense, the proposed approach is an alternative to grid-based techniques such as based on the level-set method [22]. In order to illustrate this new framework, in this paper we solve a design (inverse) problem for a vortex system in equilibrium with solid boundaries described by the 2D steady-state Euler equations. The structure of the paper is as follows: in the next Section we introduce a class of steady-state solutions of 2D Euler equations known as the Prandtl–Batchelor flows which will be used as our model vortex system, in the following Section we formulate the vortex design problem mathematically, in Section 4 we introduce elements of the shape calculus and establish the optimization framework, in Section 5 we discuss some numerical aspects of the solution of the optimization problem, whereas the computational results are presented in Section 6; discussion and conclusions are deferred to Sections 7 and 8, respectively.

2 Prandtl–Batchelor Flow as a Model Vortex System

As is well known [23, 24, 25], the streamfunction ψ in the 2D steady–state Euler flows satisfies the following boundary value problem

$$\Delta\psi = f(\psi) \quad \text{in } \Omega, \quad (1a)$$

$$\psi = \psi_b \quad \text{on } \partial\Omega, \quad (1b)$$

where $\Omega \subset \mathbb{R}^2$ is the flow domain, whereas $\psi_b : \partial\Omega \rightarrow \mathbb{R}$ is the boundary value of the streamfunction consistent with the prescribed boundary condition V_b^n for the wall–normal velocity component, i.e., $V_b^n \triangleq \mathbf{v} \cdot \mathbf{n}|_{\partial\Omega} = \frac{\partial\psi}{\partial s}|_{\partial\Omega}$ in which $\mathbf{v} = [u, v] \triangleq \left[\frac{\partial\psi}{\partial y}, -\frac{\partial\psi}{\partial x} \right]$, \mathbf{n} is the unit vector normal to $\partial\Omega$ and pointing into the domain Ω , and s is the arc–length coordinate along $\partial\Omega$ (the symbol “ \triangleq ” means “equal to by definition”). The function $f : \mathbb{R} \rightarrow \mathbb{R}$ is not a priori prescribed and must only meet some rather mild regularity criteria [24]. We note that its indeterminacy is a signature of the lack of uniqueness of solutions of the Euler equations. A common choice of the function f , motivated by the Prandtl–Batchelor hypothesis [26, 27], is as follows

$$f(\psi) = -\omega H(\psi_0 - \psi), \quad (2)$$

where $\omega, \psi_0 \in \mathbb{R}$ are two parameters and $H(\cdot)$ is the Heaviside function. We remark that with the form of $f(\psi)$ given in (2), the solutions of (1) feature regions of constant vorticity ω bounded by the streamline with $\psi = \psi_0$ and embedded in an otherwise irrotational (potential) flow (region A in Figure 1). Evidently, solutions to (1)–(2) are characterized by two parameters, ω and ψ_0 , or equivalently, the circulation of the vortex $\Gamma \triangleq \omega \int_{\Omega} H(\psi_0 - \psi) d\Omega$ and its area $|A| \triangleq \int_{\Omega} H(\psi_0 - \psi) d\Omega$. In addition to an analytical solution of (1)–(2) available in the form of the Rankine vortex [24], two–parameter families of solutions were found numerically, for example, by Pierrehumbert [28] for a counter–rotating vortex pair in an unbounded domain, and by Elcrat et al. [29] for the case of two counter–rotating vortices in equilibrium with a circular cylinder and an uniform flow at infinity. By fixing the circulation Γ of an individual vortex in these solutions, one obtains a family of flows desingularizing, respectively, a pair of point vortices and the Föppl system [30], which are recovered in the limit $|A| \rightarrow 0$ (or, equivalently, $\omega \rightarrow \pm\infty$). One such family of solutions of (1)–(2) desingularizing the Föppl system computed originally by Elcrat et al. [29] is shown in Figure 2. Some questions concerning the conditions under which solutions of (1)–(2) can be continued with respect to their parameters were recently addressed in [31]. Hereafter we will only consider problems with zero net mass flux across the domain boundary $\partial\Omega$, so that the boundary data ψ_b must satisfy the

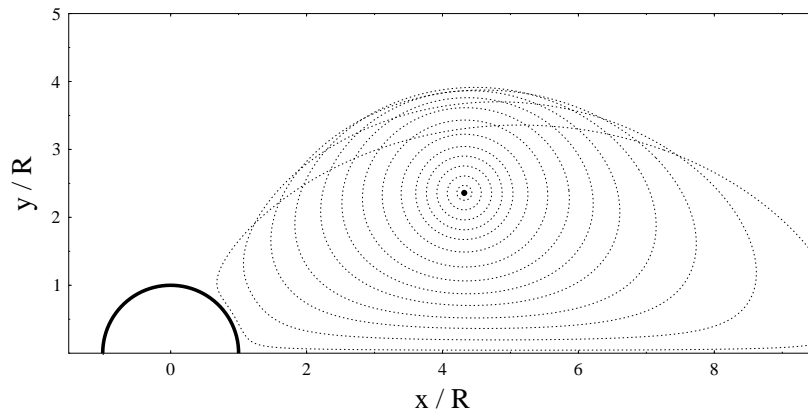


Fig. 2. (Dotted lines) boundaries of the vortex patches with different areas $|A|$ obtained by Elcrat et al. [29] as solutions of (1)–(2) desingularizing the Föppl point–vortex equilibrium [30] represented by the dot. The solid line represents the obstacle.

condition

$$\int_{\partial\Omega} \frac{\partial\psi_b}{\partial s} ds = \int_{\partial\Omega} \mathbf{v} \cdot \mathbf{n} ds = 0. \quad (3)$$

For some technical reasons (cf. [31]) we will assume that the vortex boundary ∂A is smooth, however, the boundary of the flow domain $\partial\Omega$ may have corners, although cusps are not allowed. There are also no restrictions on the connectivity of the flow domain Ω .

As is evident from Figure 2, Euler flows characterized by finite–area vortices have qualitatively quite different properties than the limiting point–vortex systems. We emphasize that the point–vortex systems have in fact the form of *finite–dimensional* dynamical systems, hence the solution of control and optimization problems is based on application of the finite–dimensional theory which is, at least in principle, a straightforward task [19]. For example, a related optimal control problem for the Föppl point vortex system was thoroughly investigated in [32]. On the other hand, Euler flows with finite–area vortices can be regarded as *infinite–dimensional* dynamical systems. Furthermore, we can rewrite equations (1)–(2) in the following equivalent form

$$\Delta\psi_1 = -\omega \quad \text{in } A(\psi_b), \quad (4a)$$

$$\Delta\psi_2 = 0 \quad \text{in } \Omega \setminus \bar{A}(\psi_b), \quad (4b)$$

$$\psi_1 = \psi_2 = \psi_0 \quad \text{on } \partial A(\psi_b), \quad (4c)$$

$$\frac{\partial\psi_1}{\partial n} = \frac{\partial\psi_2}{\partial n} \quad \text{on } \partial A(\psi_b), \quad (4d)$$

$$\psi_2 = \psi_b \quad \text{on } \partial\Omega, \quad (4e)$$

where $\psi_1 = \psi|_{A(\psi_b)}$ and $\psi_2 = \psi|_{\Omega \setminus \bar{A}(\psi_b)}$ are the restrictions of the streamfunction ψ to, respectively, the rotational and irrotational part of the flow and \mathbf{n} is the unit vector normal to the vortex boundary ∂A and directed into A (although \mathbf{n} was earlier defined as the unit vector normal to $\partial\Omega$, despite this abuse of notation, it is clear from the context which normal vector is meant). Representation (4) makes it clear that (1)–(2) is in fact a free–boundary problem, i.e., one in which the shape of the vortex boundary ∂A needs to be determined as a part of the solution of the problem. In order to highlight this fact we used the notation $A(\psi_b)$ emphasizing the dependence of the shape of the vortex region on the boundary condition ψ_b which will serve as our “control variable”. System (4) will be used in our analysis alongside the more common formulation (1)–(2). As will become evident below, dealing with systems of the free–boundary type in the context of optimal control problems is a subtle issue and will require the use of the shape calculus [20, 21] in combination with the standard adjoint–based analysis [11]. The specific problem we will address as an illustration of the general approach can be formulated as follows

Problem 1 (Vortex Design) *Determine the boundary condition ψ_b satisfying constraint (3) such that solutions of system (4) will be characterized by vortex region(s) $A(\psi_b)$ with the prescribed shape $\partial\tilde{A}$, area $|\tilde{A}|$ and circulation Γ .*

Such vortex design problem is relevant to applications in aerodynamics, where it is often desirable to contain the vorticity to some specific parts of the flow domain, for instance, in order to avoid interference with other objects present in the wake. We remark that the Euler flows discussed above, both with and without control, are subject to D’Alembert’s paradox [33], as they generate no drag force. However, in asymmetric configurations Euler flows may have a nonzero lift, and such flows are of constant interest in aerodynamics (e.g., the “Kasper wing” with vortices trapped in a cavity on the upper side of the aerofoil [34, 35, 36]). There also exist steady Euler flows which are not subject to D’Alembert’s paradox, and the Kirchhoff free–streamline flow is one example [37]. Other possible applications arise in the context of combustion phenomena where it is often useful to manipulate the location and shape of the strongly mixing vortical regions of the flow in order to ensure that the reactants are suitably mixed [38].

3 Statement of Vortex Design Problem

In this Section we provide a precise mathematical formulation of the vortex design problem. Suppose we are interested in obtaining an Euler flow with the same circulation Γ and area $|A|$ of the vortex as in one of the solutions shown in Figure 2, but with a different geometry, i.e., location and shape, of the vortex region A . The problem of

vortex design consists then in determining the boundary condition ψ_b in (1b) such that the geometry of the resulting vortex region $A(\psi_b)$ is as close as possible in a suitably-defined sense to the desired geometry. We now proceed to define a measure of “closeness” of two vortex regions, namely, the prescribed region \tilde{A} and the actually obtained region A . Since vortex patches are geometric objects, this is not quite straightforward. In the first place, we reiterate that solutions of (4) represent a two-parameter family of flows, hence in order to allow the prescribed and obtained vortex regions to be exactly the same, they must correspond to the same values of the parameters Γ and $|A|$. Thus, we will consider the parameters Γ and $|A|$ fixed in the optimization process and equal to the values characterizing the prescribed vortex region \tilde{A} . Closeness of two contours will be quantified using a cost functional $j : \mathcal{X} \times \mathcal{Y} \rightarrow \mathbb{R}$, where \mathcal{X} and \mathcal{Y} are the function spaces made up of, respectively, functions representing the boundary conditions ψ_b which satisfy (3) and the solutions ψ . It might be tempting to define the cost functional j based on the (unsigned) area $|\Delta A(\psi_b, \psi)|$ enclosed between the two contours $A(\psi_b, \psi)$ and \tilde{A} , see Figure 3. In such case, the expression for the cost functional $j(\psi_b, \psi)$ would take the following form (for consistency with the subsequent statement of the constrained optimization problem both the control ψ_b and the state ψ are indicated as variables)

$$j(\psi_b, \psi) = \frac{1}{2} \iint_{|\Delta A(\psi_b, \psi)|} dx dy. \quad (5)$$

We remark, however, that the unsigned area $|\Delta A(\psi_b, \psi)|$ is rather difficult to compute numerically, as it requires one to keep track of all the intersection points of the contours $A(\psi_b, \psi)$ and \tilde{A} , and adjust the orientation of the normal vector in order to ensure that the computed area is always positive. Thus, we propose an alternative definition of the cost functional $j(\psi_b, \psi)$. It is based on the fact, see, e.g., [39, 40], that every smooth planar region is uniquely characterized by its (infinite) set of moments defined as

$$M_n(A) \triangleq \int_A (z - z_0)^n dA = \frac{i}{2(n+1)} \oint_{\partial A} (z - z_0)^{n+1} d\bar{z}, \quad n = 0, 1, \dots, \quad (6)$$

where for the sake of compactness we used the complex notation with $z \triangleq x + iy$, $i \triangleq \sqrt{-1}$, an overbar representing the complex conjugation and z_0 denoting an arbitrarily chosen origin. We note that the contour integral in (6) is obtained from the area integral defining M_n via the application of complex Green’s theorem. We emphasize that, as a result of this transformation, the moments M_n can be computed numerically quite easily as contour integrals. It should be noted that the moments M_n for small values of n admit a straightforward geometric interpretation, namely, $M_0(A)$ represents the area of the region A , $M_1(A)$ is related to its centroid, $M_2(A)$ is related to its eccentricity, etc. Denoting $\tilde{M}_1, \dots, \tilde{M}_N$ the first N moments of the prescribed contour \tilde{A} , we then obtain

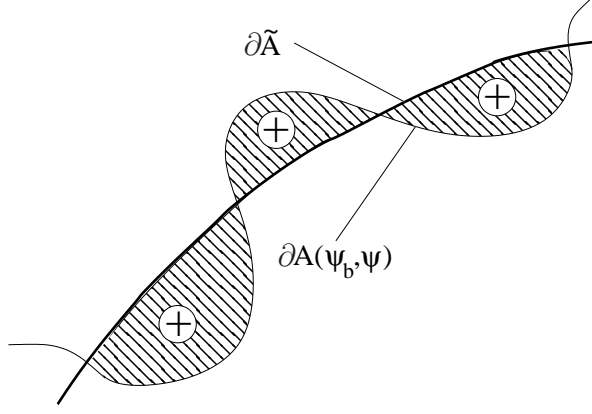


Fig. 3. Sketch illustrating the definition of the *unsigned* area $|\Delta A(\psi_b, \psi)|$ enclosed between the boundaries of the prescribed region \tilde{A} and the region $A(\psi_b, \psi)$ obtained in the solution ψ with the boundary condition ψ_b .

the following expression for the cost functional

$$j(\psi_b, \psi) = \frac{1}{2} \sum_{n=1}^N \alpha_n [M_n(\psi_b, \psi) - \tilde{M}_n]^2, \quad (7)$$

where the weights $\alpha_1, \dots, \alpha_N \in \mathbb{R}^+$ were introduced to control the relative importance of the different moments in the optimization process. We will use expression (7) in our subsequent developments as a measure of the closeness of the two contours $A(\psi_b, \psi)$ and \tilde{A} . We note that the moments corresponding to $n = 0$ are not included in (7). The reason is that, in view of our assumption made above about the fixed contour area, $M_0(\psi_b, \psi) \equiv \tilde{M}_0 \equiv |A|$. We also add that optimization problems cast in terms of functionals (5) and (7) are not quite meaningful for point vortices as they possess no shape.

Finally, our problem of vortex design can be stated formally as follows

$$\begin{aligned} \{\hat{\psi}_b, \hat{\psi}\} &= \underset{\psi_b \in \mathcal{X}, \psi \in \mathcal{Y}}{\operatorname{argmin}} j(\psi_b, \psi) \\ \text{subject to: } &(4), \\ &\omega \int_{\Omega} H(\psi_0 - \psi) d\Omega = \Gamma, \\ &\int_{\Omega} H(\psi_0 - \psi) d\Omega = |A|, \end{aligned} \quad (8)$$

where $j(\psi_b, \psi)$ is given in (7), Γ and $|A|$ are specified (fixed) parameters, whereas $\hat{\psi}_b$ and $\hat{\psi}$ are the optimal control, i.e., the optimal boundary condition in (1b), and the optimal state, i.e., the solution (streamfunction) of governing equation (1a) corresponding to the optimal boundary condition. We remark that *constrained* formulation (8) implies

simultaneous minimization with respect to the control ψ_b and the state variable ψ . Since discretizations of the latter variable are typically characterized by a very large dimension, computational solution of (8) is rather inconvenient. In such situations it is customary to transform constrained formulation (8) into the corresponding *unconstrained* formulation. Under suitable assumptions on solutions of system (4), cf. [31], and with all parameters held fixed, we can write $\psi = \psi(\psi_b)$ which allows us to define the *reduced* cost functional as follows [41]

$$\mathcal{J}(\psi_b) \triangleq j(\psi_b, \psi(\psi_b)), \quad (9)$$

where $j(\cdot, \cdot)$ is given in (7). Thus, the equivalent *unconstrained* formulation of vortex design problem (8) is

$$\hat{\psi}_b = \operatorname{argmin}_{\psi_b \in \mathcal{X}} \mathcal{J}(\psi_b). \quad (10)$$

We observe that now the constraints are “hidden” in the dependence of the state variable ψ on the control variable ψ_b . Thus, hereafter we will change the arguments (ψ_b, ψ) to (ψ_b) in other variables as well. From the computational point of view, formulation (10) is preferable to formulation (8), since now minimization is performed with respect to the control variable ψ_b only.

To set the tone for the subsequent discussion, we now briefly outline our gradient-based approach to solution of problem (10). We note that the minimizers $\hat{\psi}_b$ are characterized by the vanishing of the Gâteaux differential $\mathcal{J}'(\psi_b; \psi'_b) \triangleq \lim_{\epsilon \rightarrow 0} \epsilon^{-1} [\mathcal{J}(\psi_b + \epsilon \psi'_b) - \mathcal{J}(\psi_b)]$ for all perturbation variables $\psi'_b \in \mathcal{X}$ [42], i.e.,

$$\forall_{\psi'_b \in \mathcal{X}} \quad \mathcal{J}'(\hat{\psi}_b; \psi'_b) = 0. \quad (11)$$

Such minimizers can be found as $\hat{\psi}_b = \lim_{k \rightarrow \infty} \psi_b^{(k)}$ by employing the following gradient descent approach

$$\begin{cases} \psi_b^{(k+1)} = \psi_b^{(k)} - \tau^{(k)} \nabla \mathcal{J}(\psi_b^{(k)}), & k = 1, \dots, \\ \psi_b^{(1)} = \psi_{b,0}, \end{cases} \quad (12)$$

in which the index k represents the iteration count, $\nabla \mathcal{J}(\psi_b)$ is the gradient of cost functional $\mathcal{J}(\psi_b)$ with respect to the control variable ψ_b , $\tau^{(k)}$ is the length of the step along the descent direction at the k -th iteration, whereas $\psi_{b,0}$ is the initial guess. For the sake of clarity, formulation (12) corresponds to the steepest-descent algorithm, however, in practice one typically uses more advanced minimization techniques, such as the conjugate gradient method, or one of the quasi-Newton techniques [41]. We remark that it is not obvious whether the vortex design problem defined in Section 1 admits an exact solution in the sense that there exists a boundary condition $\hat{\psi}_b$ such that $A(\hat{\psi}_b)$ and \tilde{A} coincide, so that $\mathcal{J}(\hat{\psi}_b) = 0$ for any given target contour \tilde{A} . Establishing the

existence of such a control would require advanced methods of mathematical analysis and is outside the scope of this paper. As implied by optimization formulations (8) and (10), we will content ourselves with finding least-squares solutions of the vortex design problem. Moreover, we also note that, since minimization problem (10) is in general nonconvex, condition (11) characterizes only a local, rather than global, minimizer. We should emphasize here that the present optimization problem in practice is not amenable to treatment using high-level optimization routines available in computing environments such as MATLAB (we will elaborate more on the reasons in Section 8). Thus, in the next Section we proceed to discuss the calculation of the cost functional gradient $\nabla \mathcal{J}(\psi_b)$ which is a critical ingredient of minimization algorithm (12).

4 Optimization Framework for a Free-Boundary Problem

Our main goal in this Section is to obtain an expression for the cost functional gradient $\nabla \mathcal{J}(\psi_b)$ which could be used in iterative algorithm such as (12). Given an expression for the Gâteaux differential $\mathcal{J}'(\psi_b; \psi'_b)$, the gradient can be extracted by employing the Riesz representation theorem [43]

$$\forall_{\psi'_b \in \mathcal{X}} \quad \mathcal{J}'(\psi_b; \psi'_b) = \langle \nabla \mathcal{J}(\psi_b), \psi'_b \rangle_{\mathcal{X}}, \quad (13)$$

where $\langle \cdot, \cdot \rangle_{\mathcal{X}}$ denotes the inner product in the Hilbert space \mathcal{X} . Our first step is therefore to compute the Gâteaux differential of the reduced form of cost functional (7). We observe that the moments $M_n(A)$, $n = 1, \dots, N$ are expressed in terms of contour integrals (6) defined on the level sets $\psi = \psi_0$ of solutions of the governing equation, cf. (4c). The main challenge in differentiating such integrals is to identify how the contour ∂A (i.e., the vortex boundary) changes as a result of perturbing the boundary condition in (1). This is properly dealt with using the methods of the shape calculus [20, 21]. The first step is to construct a suitable parameterization of the shape of the vortex region. This is done by representing points $\mathbf{x}(\tau, \mathbf{x}')$ on the perturbed vortex boundary $\partial A(\tau, \mathbf{x}')$ as

$$\mathbf{x}(\tau, \mathbf{x}') = \mathbf{x} + \tau \mathbf{x}'. \quad \text{for } \forall_{\mathbf{x} \in \partial A(0)}, \quad (14)$$

where τ is a real parameter, $\partial A(0)$ is the original unperturbed vortex boundary and \mathbf{x}' is a “velocity” field characterizing the perturbation. We will use the notation $A(0) \triangleq A(0, \mathbf{x}')$ and $\partial A(0) \triangleq \partial A(0, \mathbf{x}')$ for the vortex region and its boundary, respectively. The Gâteaux shape differential of moments (6) with respect to the shape of the vortex region A and

computed in the direction of the perturbation field \mathbf{x}' is thus expressed as

$$M'_n(A(0); \mathbf{x}') = \lim_{\tau \rightarrow 0} \tau^{-1} [M_n(A(\tau, \mathbf{x}')) - M_n(A(0))], \quad n = 1, \dots, N. \quad (15)$$

Out of the two expressions for the moment M_n in (6), the first one (given in terms of the area integral) leads to somewhat simpler calculations. Its shape differential can be determined using a classical result concerning shape differentiation [21] which says that for a smooth function G defined on a smooth region A

$$\left(\int_{A(\tau, \mathbf{x}')} G d\Omega \right)' = \int_{A(0)} G' d\Omega + \oint_{\partial A(0)} G(\mathbf{x}' \cdot \mathbf{n}) ds, \quad (16)$$

where the prime denotes the shape derivative defined as in (15). Applying formula (16) to (6), we thus obtain

$$M'_n(A(0); \mathbf{x}') = \oint_{\partial A(0)} (z - z_0)^n (\mathbf{x}' \cdot \mathbf{n}) ds, \quad n = 1, \dots, N, \quad (17)$$

and then for the Gâteaux differential of the reduced cost functional $\mathcal{J}(\psi_b)$

$$\begin{aligned} \mathcal{J}'(\psi_b; \psi'_b) &= \sum_{n=1}^N \left\{ \alpha_n \operatorname{Re}[M_n(A(\psi_b)) - \tilde{M}_n] \oint_{\partial A(0)} \operatorname{Re}[(z - z_0)^n] (\mathbf{x}' \cdot \mathbf{n}) ds \right\} \\ &+ \sum_{n=1}^N \left\{ \alpha_n \operatorname{Im}[M_n(A(\psi_b)) - \tilde{M}_n] \oint_{\partial A(0)} \operatorname{Im}[(z - z_0)^n] (\mathbf{x}' \cdot \mathbf{n}) ds \right\}. \end{aligned} \quad (18)$$

We observe that the perturbation “velocity” field \mathbf{x}' is in fact not arbitrary, but represents the displacement of the vortex boundary ∂A resulting from perturbing the boundary condition on $\partial\Omega$ in free-boundary problem (4). The perturbations \mathbf{x}' and ψ'_b can be related by considering interface condition (4c) which after shape-differentiation yields [44]

$$\psi' \Big|_{\partial A(0)} + \frac{\partial \psi}{\partial n} \Big|_{\partial A(0)} (\mathbf{x}' \cdot \mathbf{n}) = \psi'_0 = 0, \quad (19)$$

where we denoted $\psi' \Big|_{\partial A(0)} \triangleq \psi'_1 \Big|_{\partial A(0)} = \psi'_2 \Big|_{\partial A(0)}$ and $\frac{\partial \psi}{\partial n} \Big|_{\partial A(0)} \triangleq \frac{\partial \psi_1}{\partial n} \Big|_{\partial A(0)} = \frac{\partial \psi_2}{\partial n} \Big|_{\partial A(0)}$.

From (19) we obtain

$$\mathbf{x}' \cdot \mathbf{n} = - \left(\frac{\partial \psi}{\partial n} \Big|_{\partial A(0)} \right)^{-1} \psi' \Big|_{\partial A(0)} \quad (20)$$

which allows us to transform Gâteaux differential (18) as follows

$$\begin{aligned} \mathcal{J}'(\psi_b; \psi'_b) = & - \sum_{n=1}^N \left\{ \alpha_n \operatorname{Re}[M_n(\psi_b) - \tilde{M}_n] \oint_{\partial A(0)} \left(\frac{\partial \psi}{\partial n} \Big|_{\partial A(0)} \right)^{-1} \operatorname{Re}[(z - z_0)^n] \psi' \Big|_{\partial A(0)} ds \right\} \\ & - \sum_{n=1}^N \left\{ \alpha_n \operatorname{Im}[M_n(\psi_b) - \tilde{M}_n] \oint_{\partial A(0)} \left(\frac{\partial \psi}{\partial n} \Big|_{\partial A(0)} \right)^{-1} \operatorname{Im}[(z - z_0)^n] \psi' \Big|_{\partial A(0)} ds \right\}. \end{aligned} \quad (21)$$

The perturbation streamfunction ψ' is the solution of the following perturbation system obtained by shape-differentiating free-boundary problem (4), see [44],

$$\Delta \psi'_1 = 0 \quad \text{in } A(\psi_b), \quad (22a)$$

$$\Delta \psi'_2 = 0 \quad \text{in } \Omega \setminus \bar{A}(\psi_b), \quad (22b)$$

$$\psi'_1 = \psi'_2 = \psi' \quad \text{on } \partial A(\psi_b), \quad (22c)$$

$$\frac{\partial \psi'_1}{\partial n} - \frac{\partial \psi'_2}{\partial n} = -\omega \left(\frac{\partial \psi}{\partial n} \Big|_{\partial A(0)} \right)^{-1} \psi' \quad \text{on } \partial A(\psi_b), \quad (22d)$$

$$\psi'_2 = \psi'_b \quad \text{on } \partial \Omega. \quad (22e)$$

We clarify that condition (22d) is obtained by first shape-differentiating relation (4d) which yields

$$\frac{\partial \psi'_1}{\partial n} + \frac{\partial^2 \psi_1}{\partial n^2} (\mathbf{x}' \cdot \mathbf{n}) = \frac{\partial \psi'_2}{\partial n} + \frac{\partial^2 \psi_2}{\partial n^2} (\mathbf{x}' \cdot \mathbf{n}) \quad \text{on } \partial A(\psi_b). \quad (23)$$

Then, using (4a)–(4b) with the assumption that the solutions ψ_1 and ψ_2 are smooth up to the boundary $\partial A(0)$, and rewriting the Laplace operator in the local curvilinear coordinate system as $\Delta = \frac{\partial^2}{\partial n^2} + \frac{\partial^2}{\partial s^2} + \varkappa \frac{\partial}{\partial n}$, where s is the arc-length coordinate along the vortex boundary $\partial A(\psi_b)$ (cf. Figure 1) and \varkappa is the curvature of the vortex boundary, we obtain

$$(-\omega = \Delta \psi_1) \longrightarrow \frac{\partial^2 \psi_1}{\partial n^2} \Big|_{\partial A(0)} + \varkappa \frac{\partial \psi_1}{\partial n} \Big|_{\partial A(0)} \quad \text{for } \mathbf{x} \rightarrow \mathbf{x}_{\partial A} \in \partial A(0), \quad \mathbf{x} \in A(0), \quad (24a)$$

$$(0 = \Delta \psi_2) \longrightarrow \frac{\partial^2 \psi_2}{\partial n^2} \Big|_{\partial A(0)} + \varkappa \frac{\partial \psi_2}{\partial n} \Big|_{\partial A(0)} \quad \text{for } \mathbf{x} \rightarrow \mathbf{x}_{\partial A} \in \partial A(0), \quad \mathbf{x} \in \Omega \setminus \bar{A}(0), \quad (24b)$$

where we noted that $\frac{\partial^2 \psi_1}{\partial s^2} = \frac{\partial^2 \psi_2}{\partial s^2} \equiv 0$ on $\partial A(0)$, because $\psi_1 = \psi_2 = \psi_0$ on $\partial A(0)$. Condition (22d) is finally obtained combining (4d), (20), (23) and (24). We reiterate that in shape-differentiating system (4) we treated the parameters ω and ψ_0 as constants.

We remark that at this point Gâteaux differential (21) does not have the form consistent with Riesz representation formula (13), because the control perturbation ψ'_b does not appear in (21) explicitly; on the other hand, expression (21) contains $\psi'|_{\partial A(0)}$ which is related to ψ'_b through perturbation system (22). As is well known [11], the Gâteaux differential can be transformed to the Riesz form with the help of the adjoint variable ψ^* . Multiplying (22a) and (22b) by $\psi_1^* \triangleq \psi^*|_{A(0)}$ and $\psi_2^* \triangleq \psi^*|_{\Omega \setminus \bar{A}(0)}$, then integrating, respectively, over $A(0)$ and $\Omega \setminus \bar{A}(0)$, we obtain

$$\begin{aligned}
0 &= \int_{A(0)} (\Delta \psi'_1) \psi_1^* d\Omega + \int_{\Omega \setminus \bar{A}(0)} (\Delta \psi'_2) \psi_2^* d\Omega \\
&= \int_{A(0)} \psi'_1 (\Delta \psi_1^*) d\Omega + \int_{\Omega \setminus \bar{A}(0)} \psi'_2 (\Delta \psi_2^*) d\Omega \\
&\quad + \oint_{\partial A(0)} \left(\frac{\partial \psi'_1}{\partial n} - \frac{\partial \psi'_2}{\partial n} \right) \psi^* - \left(\frac{\partial \psi_1^*}{\partial n} - \frac{\partial \psi_2^*}{\partial n} \right) \psi' ds - \oint_{\partial \Omega} \frac{\partial \psi'_2}{\partial n} \psi_2^* - \frac{\partial \psi_2^*}{\partial n} \psi'_2 ds \\
&= \int_{A(0)} \psi'_1 (\Delta \psi_1^*) d\Omega + \int_{\Omega \setminus \bar{A}(0)} \psi'_2 (\Delta \psi_2^*) d\Omega \\
&\quad - \oint_{\partial A(0)} \left[\left(\frac{\partial \psi_1^*}{\partial n} - \frac{\partial \psi_2^*}{\partial n} \right) + \omega \left(\frac{\partial \psi}{\partial n} \Big|_{\partial A(0)} \right)^{-1} \psi^* \right] \psi' dx \\
&\quad + \oint_{\partial \Omega} \frac{\partial \psi_2^*}{\partial n} \psi'_b ds - \oint_{\partial \Omega} \frac{\partial \psi'_2}{\partial n} \psi_2^* ds,
\end{aligned} \tag{25}$$

where we subsequently used Green's theorem and boundary conditions (22d)–(22e). We now define the adjoint system as follows

$$\Delta \psi_1^* = 0 \quad \text{in } A(\psi_b), \tag{26a}$$

$$\Delta \psi_2^* = 0 \quad \text{in } \Omega \setminus \bar{A}(\psi_b), \tag{26b}$$

$$\psi_1^* = \psi_2^* = \psi^* \quad \text{on } \partial A(\psi_b), \tag{26c}$$

$$\begin{aligned}
\frac{\partial \psi}{\partial n} \Big|_{\partial A(0)} \left(\frac{\partial \psi_1^*}{\partial n} - \frac{\partial \psi_2^*}{\partial n} \right) + \omega \psi^* &= \sum_{n=1}^N \alpha_n \operatorname{Re}[M_n(\psi_b) - \tilde{M}_n] \operatorname{Re}[(z - z_0)^n] \\
&\quad + \sum_{n=1}^N \alpha_n \operatorname{Im}[M_n(\psi_b) - \tilde{M}_n] \operatorname{Im}[(z - z_0)^n], \quad \text{on } \partial A(\psi_b),
\end{aligned} \tag{26d}$$

$$\psi_2^* = 0 \quad \text{on } \partial \Omega, \tag{26e}$$

where the expression on the right-hand side (RHS) in (26d) results from the form of

(21). The judicious choice of boundary conditions (26d) and (26e) allows us to reduce identity (25) to the form

$$\mathcal{J}'(\psi_b; \psi'_b) = \oint_{\partial\Omega} \frac{\partial\psi_2^*}{\partial n} \psi'_b ds \quad (27)$$

which is now consistent with Riesz representation (13). Indeed, identifying \mathcal{X} with $L_2(\partial\Omega)$, i.e., the space of functions square-integrable on $\partial\Omega$, we obtain

$$\nabla\mathcal{J}(\psi_b) = \frac{\partial\psi_2^*}{\partial n} \quad \text{on } \partial\Omega \quad (28)$$

as an expression for the (reduced) gradient of cost functional (7) with respect to the control variable ψ_b . We emphasize that this gradient represents in fact an infinite-dimensional sensitivity of the functional $\mathcal{J}(\psi_b)$ to the control variable ψ_b , and its evaluation requires solution of both direct and adjoint systems (4) and (26). We conclude by saying that first-order optimality condition (11) can equivalently be expressed as

$$\nabla\mathcal{J}(\hat{\psi}_b) = 0 \quad \text{on } \partial\Omega \quad (29)$$

which complemented with (4) and (26) forms a closed system of equations defining the optimal control $\hat{\psi}_b$, the corresponding optimal state $\hat{\psi}$ and the associated Lagrange multiplier (adjoint variable) $\hat{\psi}^*$ [42].

Up to this point, our discussion has been in fairly general terms and the results apply to finite-area vortex systems satisfying (4) in arbitrary domains Ω . In order to make the following discussion more concrete, from now on we will focus on a specific vortex design problem concerning optimization of the geometry of vortices in equilibrium with a circular cylinder in the presence of a free stream velocity $U_\infty \mathbf{e}_x$ at infinity (\mathbf{e}_x is the unit vector associated with the OX axis), cf. Figure 2. Thus, the domain boundary splits as follows $\partial\Omega = \partial B \cup \Sigma$, where ∂B is the boundary of the obstacle, whereas Σ is the domain perimeter assumed to be at infinity. Since the control ψ_b is applied at the obstacle boundary ∂B only (i.e., $\psi_b \equiv 0$ on Σ), in this particular problem one can replace $\partial\Omega$ with ∂B in (27) and (28). We are interested in configurations symmetric with respect to the flow centerline which can be constructed by solving the problem in the upper half-plane ($y \geq 0$), but including the effect of image vortices with opposite vorticity located symmetrically below the flow centerline $y = 0$. To satisfy the boundary conditions on ∂B , additional images will also be placed inside the obstacle. The system of the principal and image vortices used in this problem is shown in Figure 4.

We note that solutions of perturbation and adjoint systems (22) and (26) are functions harmonic in $A(0)$ and $\Omega \setminus \overline{A}(0)$. We will now reformulate these problems in a way that makes their numerical solution easier (as a matter of fact, solution of the perturbation

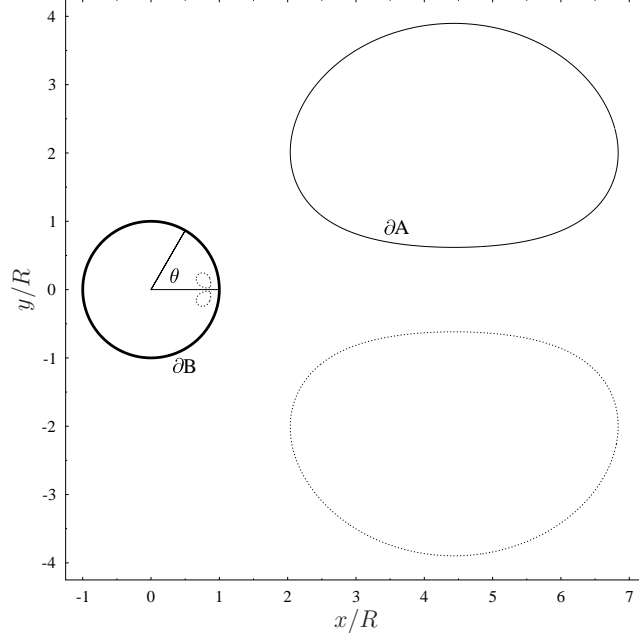


Fig. 4. (Solid line) Principal vortex A and (dotted lines) image vortices used to construct Green's function (30). The obstacle boundary is denoted ∂B .

problem is not needed to determine the cost functional gradient $\nabla \mathcal{J}$, however, for the sake of completeness, we will also include this problem in our discussion). While the original unknowns ψ' and ψ^* are defined everywhere in the domain Ω , which in the present problem is unbounded, we will recast systems (22) and (26) in terms of new unknowns, the densities of the corresponding single-layer potentials, defined on the vortex boundary ∂A only.

Using image singularities as illustrated in Figure 4 will allow us to reduce the problem to unknowns defined on the boundary ∂A of the principal vortex only. This can be done by introducing Green's function which will satisfy the boundary conditions on the obstacle boundary ∂B and be symmetric with respect to the OX axis. It can be constructed using the “circle theorem” [37] for the images inside the obstacle and the reflection principle for the images below the flow centerline, and takes the form (see also [47])

$$\begin{aligned}
 S(z, \zeta) &= S_1(z, \zeta) + S_2(z, \zeta) + S_3(z, \zeta) + S_4(z, \zeta) \\
 &= \frac{1}{2\pi} \ln |z - \zeta| - \frac{1}{2\pi} \ln |z - \bar{\zeta}| - \frac{1}{2\pi} \ln |z - \bar{\zeta}^{-1}| + \frac{1}{2\pi} \ln |z - \zeta^{-1}|,
 \end{aligned} \tag{30}$$

where $\zeta \in \partial A(0)$ is the singularity location, $z \in \Omega \setminus (\overline{A(0)} \cup \overline{A_-(0)} \cup \overline{B})$, and the complex representation was used for conciseness. We will develop this approach for adjoint system (26), as it plays a more important role in the computations of the vortex design problem; in the case of perturbation system (22) one needs to “lift” boundary condition (22e), and then follow an analogous sequence of steps. Solution ψ_2^* of (26) vanishing on ∂B [cf. (26e)] and symmetric with respect to the OX axis can be represented thus

$$\begin{aligned} \psi_2^*(z) = & \oint_{\partial A(0)} \gamma^*(\zeta) S_1(z, \zeta) ds_\zeta + \oint_{\partial A(0)} \gamma^*(\zeta) S_2(z, \zeta) ds_\zeta \\ & + \oint_{\partial A(0)} \gamma^*(\zeta) S_3(z, \zeta) ds_\zeta + \oint_{\partial A(0)} \gamma^*(\zeta) S_4(z, \zeta) ds_\zeta, \end{aligned} \quad (31)$$

where $\gamma^* : \partial A(0) \rightarrow \mathbb{R}$ is the density of the single-layer potential [45]. Taking the limit $z \rightarrow z_0 \in \partial A(0)$ and using well-known properties of the single-layer potential, we obtain

$$\psi_2^*(z_0) = \oint_{\partial A(0)} \gamma^*(\zeta) S_1(z_0, \zeta) ds_\zeta + \sum_{k=2}^4 \oint_{\partial A(0)} \gamma^*(\zeta) S_k(z_0, \zeta) ds_\zeta, \quad (32)$$

where the kernel $S_1(z_0, \zeta)$ becomes singular and the corresponding integral is to be understood in the principal-value sense [45]. Using now boundary condition (26d) and noting that the density γ^* of the single-layer potential can be expressed as $\gamma^* = \frac{\partial \psi^*}{\partial n} - \frac{\partial \psi_2^*}{\partial n}$ (see, e.g., [46]) we obtain

$$\begin{aligned} \left. \frac{\partial \psi}{\partial n} \right|_{\partial A(0)} \gamma^*(z_0) + \omega \oint_{\partial A(0)} \gamma^*(\zeta) S_1(z_0, \zeta) ds_\zeta + \omega \sum_{k=2}^4 \oint_{\partial A(0)} \gamma^*(\zeta) S_k(z_0, \zeta) ds_\zeta = \\ = \sum_{n=1}^N \alpha_n \left\{ \text{Re}[M_n(\psi_b) - \tilde{M}_n] \text{Re}[(z - z_0)^n] + \text{Im}[M_n(\psi_b) - \tilde{M}_n] \text{Im}[(z - z_0)^n] \right\} \end{aligned} \quad (33)$$

which is analogous to a Fredholm integral equation of the second type [50]. We have thus reduced elliptic boundary-value problem (26) to a boundary integral equation for the density γ^* of the single-layer potential defined on the vortex boundary ∂A . Once this density is determined, the adjoint variable ψ_2^* can be computed using representation (31). In particular, this representation can be used to evaluate cost functional gradient (28). Perturbation equation (22) can be recast in terms of a boundary integral equation with identical structure as in (33), but with a different RHS term. Numerical solution of boundary integral equation (33) is discussed in Section 5.

5 Numerical Aspects

In this Section we review the numerical techniques used to address different computational aspects of our vortex design problem, namely, the calculation of the Prandtl–Batchelor solutions of Euler equations (1)–(2) in the presence of the obstacle, solution of the adjoint system in its boundary integral formulation (33), and implementation of descent algorithm (12) to find minimizers of problem (10).

In regard to the first two problems, high accuracy of solutions is ensured by the use of suitably adapted spectral techniques. As concerns finding solutions of free–boundary problem (1)–(2), we use the approach and implementation developed by Elcrat et al. [47]. It relies on an equivalent reformulation of problem (1)–(2) motivated by the method of “contour dynamics” [10], namely

$$\mathbf{v} \cdot \mathbf{n} = 0 \quad \text{on } \partial A \quad (34)$$

which implies that the vortex boundary ∂A does not change its shape. The vortex boundary satisfying (34) is found using Newton’s method in which the boundary displacements are represented using the Fourier (spectral) interpolation [48, 49]. The spectral representation is also used to discretize the normal velocity $\mathbf{v} \cdot \mathbf{n}|_{\partial A}$ and its Jacobian using integrals of the Biot–Savart type with kernels derived from (30) and understood in the principal–value sense. Overall, this approach can be regarded as a spectrally–accurate technique for finding the fixed points of the contour dynamics equations [10]. We refer the reader to the original article [47] for further details. Analogous techniques are used to evaluate the velocity component tangent to the vortex patch boundary $\frac{\partial \psi}{\partial n}|_{\partial A(0)}$ appearing in the adjoint system.

In order to solve boundary integral equation (33) we first discretize the contour ∂A with P points evenly spaced in the arc–length coordinate $s \in [0, L]$, where L is the total length of the contour boundary, i.e.,

$$\xi_1, \dots, \xi_P \in \partial A, \text{ where } \xi_p = \mathbf{x}_{\partial A}(s_p), \quad s_p \triangleq \Delta s(p-1), \quad \Delta s \triangleq \frac{L}{P}, \quad p = 1, \dots, P. \quad (35)$$

The points ξ_1, \dots, ξ_P are represented using the complex notation. Using techniques of the spectral interpolation [48, 49], the solution of boundary integral equation (33) can be approximated as

$$\gamma^*(s) \approx \sum_{p=1}^P \gamma_p^* \mathcal{L}_p(s), \quad (36)$$

where γ_p^* , $p = 1, \dots, P$ is the value of the density of the single–layer potential at the

discrete point ξ_p , whereas $\mathcal{L}_p(s)$ is the trigonometric cardinal function (i.e., the Lagrange interpolating polynomial for the periodic domain) of order p , cf. [48]. The kernels S_2 , S_3 and S_4 in (33) are well behaved, hence the corresponding integrals are proper and can be approximated in a straightforward manner using spectral integration based on (36) which yields

$$\sum_{k=2}^4 \oint_{\partial A(0)} \gamma^*(\zeta) S_k(\xi_q, \zeta) ds_\zeta \approx \sum_{p=1}^P \mathbb{M}_{qp} \gamma_p^*, \quad q = 1, \dots, P, \quad (37)$$

where \mathbb{M} is a $P \times P$ matrix approximating the integral operator. On the other hand, the kernel S_1 is unbounded as $\zeta \rightarrow z_0$ and therefore requires special treatment. Following in this regard [50], we introduce points $\boldsymbol{\eta}(s')$ situated on a unit circle and parameterized by the rescaled arc-length coordinate $s' \triangleq \frac{2\pi}{L}s$ as in (35), so that we obtain

$$\begin{aligned} S_1(z(s'), \zeta(t')) &= \frac{1}{2\pi} \ln |z(s') - \zeta(t')| = \frac{1}{4\pi} \ln \frac{|z(s') - \zeta(t')|^2}{|\boldsymbol{\eta}(s') - \boldsymbol{\eta}(t')|^2} + \frac{1}{4\pi} \ln |\boldsymbol{\eta}(s') - \boldsymbol{\eta}(t')|^2 \\ &= \frac{1}{4\pi} \ln \frac{|z(s') - \zeta(t')|^2}{4 \sin^2 \frac{s' - t'}{2}} + \frac{1}{4\pi} \ln \left(4 \sin^2 \frac{s' - t'}{2} \right), \quad s', t' \in [0, 2\pi], \quad s' \neq t', \end{aligned} \quad (38)$$

where we used the fact that $|\boldsymbol{\eta}(s') - \boldsymbol{\eta}(t')| = 2 \sin \frac{s' - t'}{2}$ for two points on the unit circle. We note that the first expression on the RHS in (38) is now bounded as $s' \rightarrow t'$, hence the corresponding integral is proper and can be approximated using standard spectral quadratures. The principal-value integral involving the product of the kernel $\frac{1}{4\pi} \ln \left(4 \sin^2 \frac{s' - t'}{2} \right)$ with the interpolating polynomial $\mathcal{L}_p(t')$ can be evaluated analytically with the resulting expressions available in [50], so that now

$$\oint_{\partial A(0)} \gamma^*(\zeta) S_1(\xi_q, \zeta) ds_\zeta \approx \sum_{p=1}^P \mathbb{T}_{qp} \gamma_p^*, \quad q = 1, \dots, P, \quad (39)$$

where \mathbb{T} is a $P \times P$ matrix approximating as discussed above the integral operator with the singular kernel S_1 . Denoting $\mathbf{f} = \left[\frac{\partial \psi}{\partial n}(\xi_1), \dots, \frac{\partial \psi}{\partial n}(\xi_P) \right]^T$, $\mathbf{g} = [\gamma_1^*, \dots, \gamma_P^*]^T$, boundary integral equation (33) can be approximated with the following system of linear equations

$$[\text{diag}(\mathbf{f}) + \mathbb{T} + \mathbb{M}] \mathbf{g} = \mathbf{r}, \quad (40)$$

where $\text{diag}(\mathbf{f})$ is a $P \times P$ diagonal matrix with entries given by the entries of the vector

\mathbf{f} , and the entries of the vector \mathbf{r} are defined as

$$r_q \triangleq \sum_{n=1}^N \alpha_n \left\{ \operatorname{Re}[M_n(\psi_b) - \tilde{M}_n] \operatorname{Re}[(\xi_q - z_0)^n] + \operatorname{Im}[M_n(\psi_b) - \tilde{M}_n] \operatorname{Im}[(\xi_q - z_0)^n] \right\}, \quad q = 1, \dots, P. \quad (41)$$

System (40) can be solved using standard techniques, and its solution \mathbf{g} can be used in conjunction with (31) and (36) to evaluate cost functional gradient (28). We add that the cost functional gradient determined in this way is a periodic and antisymmetric function of the polar angle $\theta \in [0, 2\pi)$ characterizing the points on the cylinder boundary ∂B (Figure 4), therefore it satisfies the zero net mass flux condition separately on the upper and lower part of ∂B , i.e., $\int_0^\pi \nabla \mathcal{J}(\theta) d\theta = \int_0^{-\pi} \nabla \mathcal{J}(\theta) d\theta = 0$. This property ensures that the optimal control $\hat{\psi}_b$ found with our approach will be consistent with condition (3).

With the cost functional gradient $\nabla \mathcal{J}(\psi_b)$ approximated as above, we compute the optimal control $\hat{\psi}_b$ using the Polak–Ribiere version of the conjugate gradients algorithm [41] which is a modified version of descent algorithm (12). The length of the step $\tau^{(k)}$ at every iteration k is determined by solving a line minimization problem

$$\tau^{(k)} = \operatorname{argmin}_{\tau > 0} \mathcal{J}(\psi_b^{(k)} - \tau \nabla \mathcal{J}(\psi_b^{(k)})) \quad (42)$$

using Brent’s method [51]. The following Section offers a number of computational examples illustrating the proposed approach.

6 Computational Results

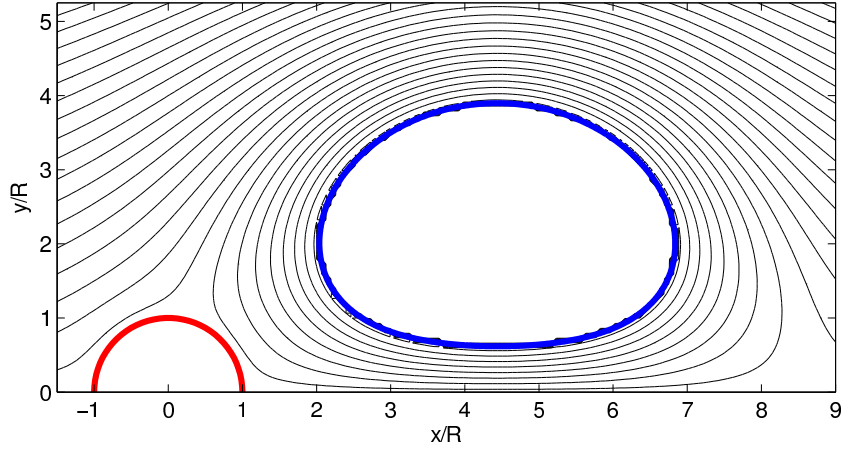
In this Section we present and analyze a number of computational results illustrating the problem of vortex design applied to the Prandtl–Batchelor flow and the proposed solution method. In the first place we will show some diagnostic tests concerning the computation of the cost functional gradients at a given iteration. Then, we will discuss subsequent iterations of the vortex design algorithm. To fix attention, we will consider a family of solutions of (1)–(2) characterized by the fixed circulation and area of the vortex, respectively, $\Gamma = 29.6$ and $|A| = 12.55$ [i.e., flows both with and without control will have the same vortex circulation and area, but different locations and shapes of the vortex region, cf. (8)]. Unless stated otherwise, in the numerical solution of boundary integral equation (33) and in the evaluation of potential (31) we use $P = 1035$ points to discretize the vortex boundary ∂A . To begin, in Figures 5a,b,c we show solutions of the direct (4) and the corresponding perturbation (22) and adjoint systems (26)

obtained at the first iteration when $\psi_b \equiv 0$ (i.e., no blowing or suction present). The perturbation streamfunction ψ' corresponds to the control perturbation $\psi'_b = \sin(\theta)$, whereas the adjoint variable ψ^* corresponds to $N = 1$ in (7) and a “target” vortex region \tilde{A} characterized by $\tilde{M}_1 = 48.973 + i28.448$. We note that the structure of the perturbation and adjoint solutions ψ' and ψ^* (Figures 5b and 5c) reflects the different ways in which the corresponding systems are “forced”: on the obstacle boundary ∂B for the perturbation system, cf. (22e), and on the vortex boundary ∂A for the adjoint system, cf. (22d). To facilitate quantitative comparisons, in this (Figure 5a) and all subsequent streamline plots (Figures 10a,b and 15a,b) isocontours of ψ are drawn corresponding to the same set of values, namely, $-4, -3.8, -3.6, \dots, 4$.

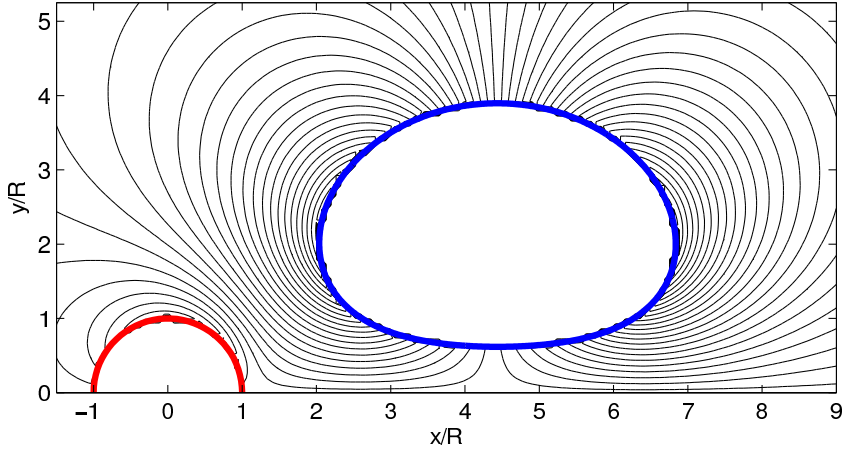
Next we proceed to analyze the consistency of the gradient $\nabla \mathcal{J}$ obtained using system (26). A standard test [52] consists in computing the Gâteaux differential (i.e., the directional derivative) of the cost functional $\mathcal{J}(\psi_b)$ in some arbitrary direction ψ'_b using relation (27) and comparing it to the result obtained with a forward finite-difference formula. Thus, deviation of the quantity $\kappa(\epsilon) \triangleq \frac{\mathcal{J}(\psi_b + \epsilon \psi'_b) - \mathcal{J}(\psi_b)}{\epsilon (\nabla \mathcal{J}, \psi'_b)}$ from the unity is a measure of the error. In Figure 6a we show the behavior of $\kappa(\epsilon)$ for a fixed perturbation ψ'_b and different discretizations of the contour ∂A . We see clearly that $\kappa(\epsilon)$ approaches the unity as the discretization is refined (i.e., as P increases). We emphasize that, since we are using the “differentiate-then-discretize” rather than “discretize-then-differentiate” approach, the gradient should not be expected to be accurate up to the machine precision [11]. In Figure 6b we show the behavior of $\kappa(\epsilon)$ for a fixed discretization with $P = 1035$ grid points on ∂A and perturbations ψ'_b with increasing wavenumbers. We observe that $\kappa(\epsilon)$ is closer to the unity for faster-varying perturbations. It should be emphasized that in all examined cases the quantity $\kappa(\epsilon)$ exhibits a well-defined plateau spanning almost 10 orders of magnitude in ϵ . The deviation of $\kappa(\epsilon)$ from the unity for very small values of ϵ is due to the arithmetic round-off errors, whereas for the large values of ϵ it is due to the truncation errors.

Having validated our calculation of cost functional gradients, we now go on to discuss the results of iterative optimization of the location and shape of the vortices. While in principle one could attempt to optimize simultaneously an arbitrary number $N > 1$ of the moments M_n , $n = 1, \dots, N$, we found that a preferable approach is to optimize one moment at a time. Therefore, we divide the problem into the following sequence of steps:

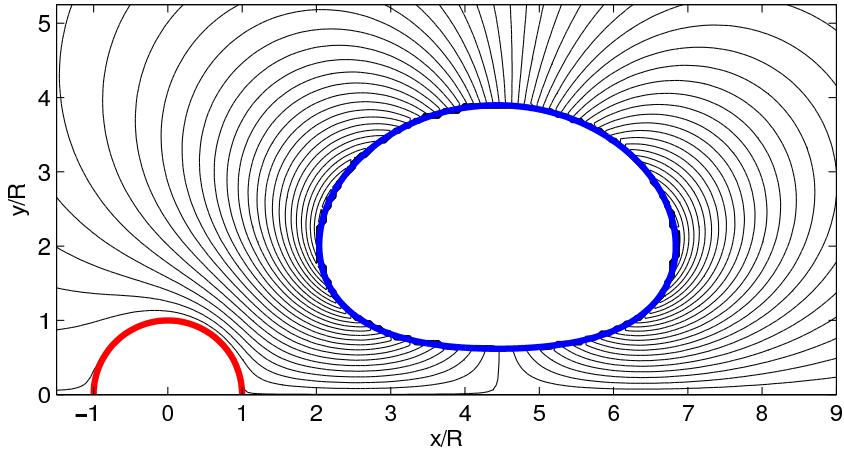
- (i) set $N = 1$ and $\alpha_1 = 1$ in cost functional (7) and solve optimization problem (10),
- (ii) shift the origin with respect to which the moments are calculated to $z_0 = \frac{\tilde{M}_1}{|A|}$, set $N = 2$, $\alpha_1 = 10$ (or some other “large” number), $\alpha_2 = 1$ in cost functional (7) and solve optimization problem (10) again, now with the optimal control $\hat{\psi}_b$ found in Step (i) used as the initial guess $\psi_{b,0}$, cf. (12),



(a)



(b)



(c)

Fig. 5. Isolines of the solutions (a) ψ of governing system (1)–(2), (b) ψ' of perturbation system (22), and (c) ψ^* of adjoint system (26). For clarity, isolines are not plotted in the interior of the vortex region A . The perturbation variable ψ' corresponds to the control perturbation $\psi'_b = \sin(\theta)$, whereas the adjoint variable ψ^* corresponds to $N = 1$ in (7) and a “target” vortex region \tilde{A} characterized by $\tilde{M}_1 = 48.973 + i28.448$.

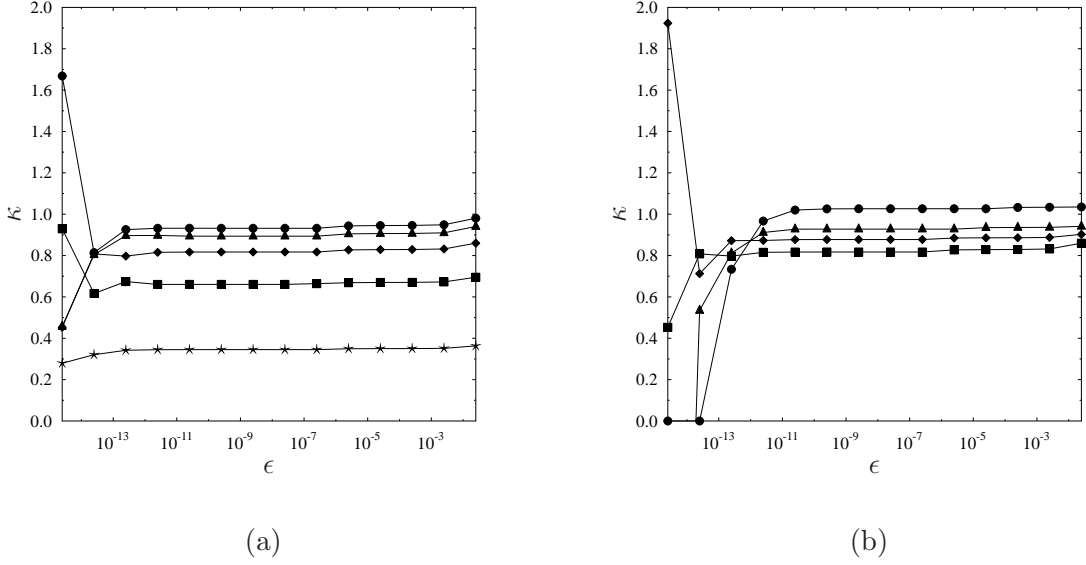


Fig. 6. Measure of the error $\kappa(\epsilon)$ in determination of the cost functional gradient for (a) a fixed control perturbation $\psi'_b = \sin(\theta)$ and different numbers of grid points discretizing the contour ∂A : (stars) $P = 131$, (squares) $P = 259$, (diamonds) $P = 519$, (triangles) $P = 1035$, (circles) $P = 2071$, and (b) for a fixed discretization with $P = 519$ and different control perturbations: (squares) $\psi'_b = \sin(\theta)$, (diamonds) $\psi'_b = \sin(2\theta)$, (triangles) $\psi'_b = \sin(3\theta)$, and (circles) $\psi'_b = \sin(4\theta)$.

- (iii) set $N = 3$, $\alpha_1 = \alpha_2 = 10$ (or some other “large” number), $\alpha_3 = 1$ in cost functional (7) and solve optimization problem (10) with the optimal control $\hat{\psi}_b$ found in the previous step used as the initial guess $\psi_{b,0}$.

Step (iii) can be repeated as many times as needed increasing each time the value of N to include all moments that need to be optimized. In regard to Step (i), we note that including the first-order moment M_1 only in the cost functional will have the effect of optimizing the centroid location of the vortex region, leaving the shape of the vortex region to change in an arbitrary manner. In regard to Step (ii), we remark that shifting the origin z_0 to the centroid of the vortex obtained in Step (i) allows for the higher-order moments M_n , $n > 1$, to have a more straightforward geometric interpretation (this issue will be discussed in greater detail further below). Setting the weights so that $\alpha_1 \gg \alpha_2$ ensures that changes to M_1 due to optimization during Step (ii) are less significant than changes to M_2 (in other words, during Step (ii) the expression $M_1(\psi_b) = \tilde{M}_1$ may be regarded as a “soft” constraint, cf. [11]). Then, when another (N -th order) moment is included in the optimization process in Step (iii), all the lower-order moments are assigned large weights $\alpha_1, \dots, \alpha_{N-1} \gg \alpha_N$ which ensures that these moments are not significantly affected by the new optimization process. The reason for proposing such an

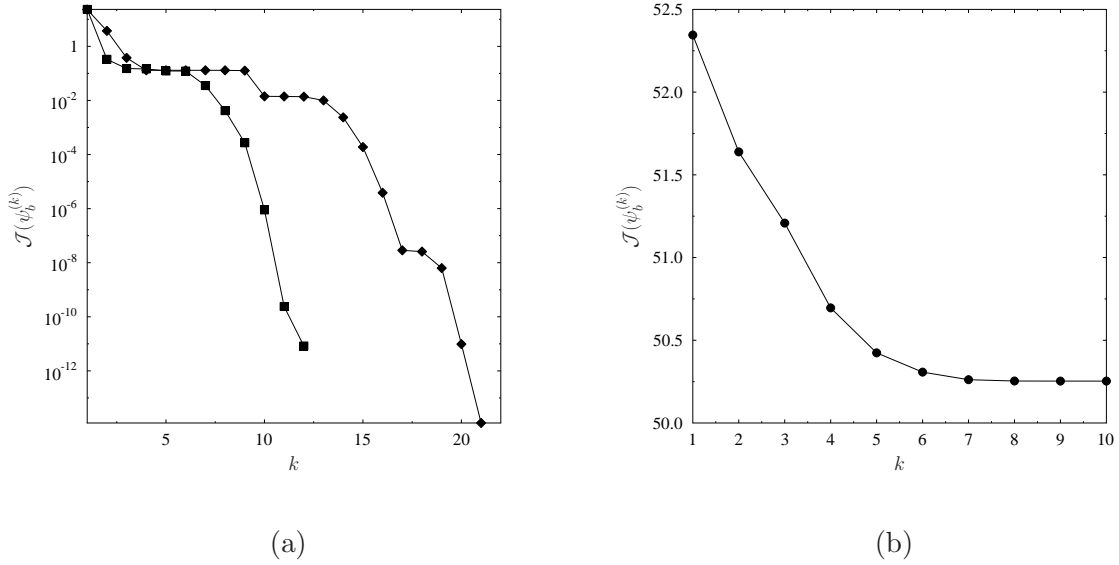
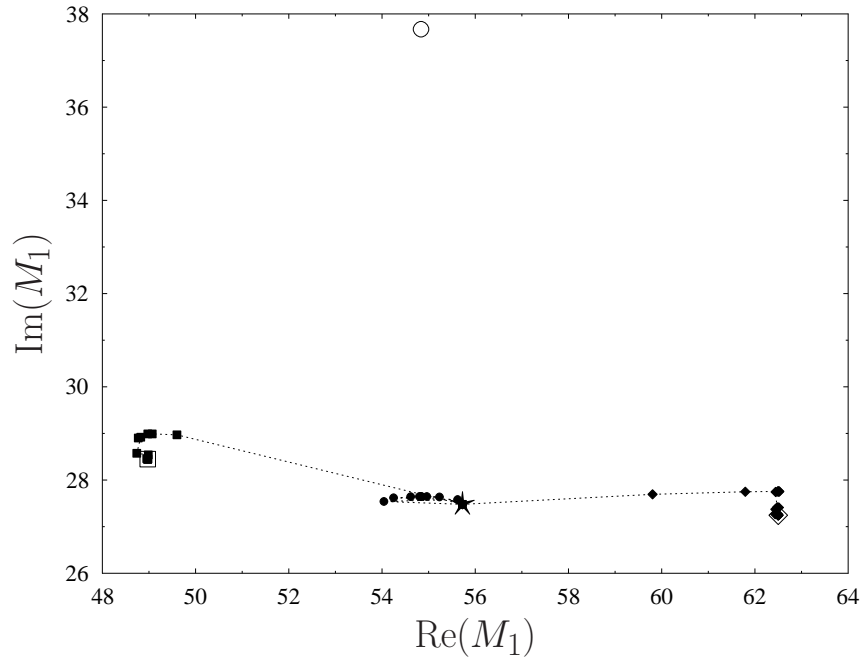


Fig. 7. Cost functional $\mathcal{J}(\psi_b^{(k)})$ as a function of the iteration count k in (a, squares) case A, (a, diamonds) case B, and (b) case C.

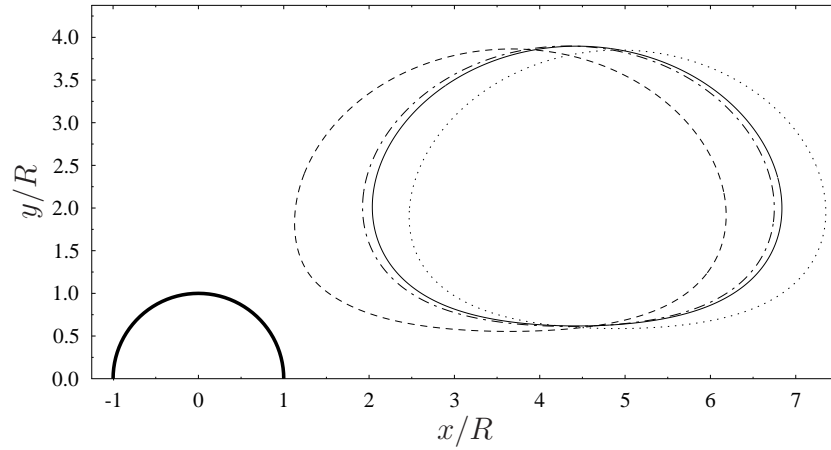
approach to the vortex design problem is that moments characterizing a contour (vortex boundary ∂A) form a hierarchy in the sense that coarser properties of the contour are encoded in the lower-order moments, whereas the higher-order moments capture finer features. Therefore, optimizing moments of order $n+1$ makes sense only when the moments of order $1, \dots, n$ already possess prescribed values. On the contrary, attempting to optimize all N moments at once might lead to a local minimum at which some lower-order moments could be far from their target values (this behavior was in fact observed in our computational experiments). We also need to emphasize that, given a prescribed set of moments $\tilde{M}_1, \dots, \tilde{M}_N$, it is not always evident that Euler system (4) will admit a solution with some boundary condition $\hat{\psi}_b$ such that the geometry of the vortex region A will match *exactly* the prescribed moments, so that $\mathcal{J}(\hat{\psi}_b) = 0$. Therefore, in the formulation of the vortex design problem we will be content with optimal solutions $\hat{\psi}_b$ for which the prescribed moments $\tilde{M}_1, \dots, \tilde{M}_N$ are matched in the least squares sense only. Below we present computations illustrating Step (i), where the first-order moment M_1 is optimized only, and Step (ii), where the second-order moment M_2 is optimized, while the first-order moment M_1 is treated as soft constraint.

In Step (i) we considered the following three cases characterized by different values of the prescribed moments:

- Case A: $\tilde{M}_1 = 48.973 + i28.448$,



(a)



(b)

Fig. 8. (a) Paths traced in the complex plane by the moments M_1 during iterations for (squares) case A, (diamonds) case B, and (circles) case C; empty symbols represent the prescribed values \tilde{M}_1 and star marks the value of M_1 at the beginning of the iterations, (b) boundaries of the vortex region A in (solid line) the flow with no control ($\psi_b \equiv 0$), (dashed line) case A, (dotted line) case B, and (dash-dotted line) case C; the thick solid line represents the obstacle boundary ∂B .

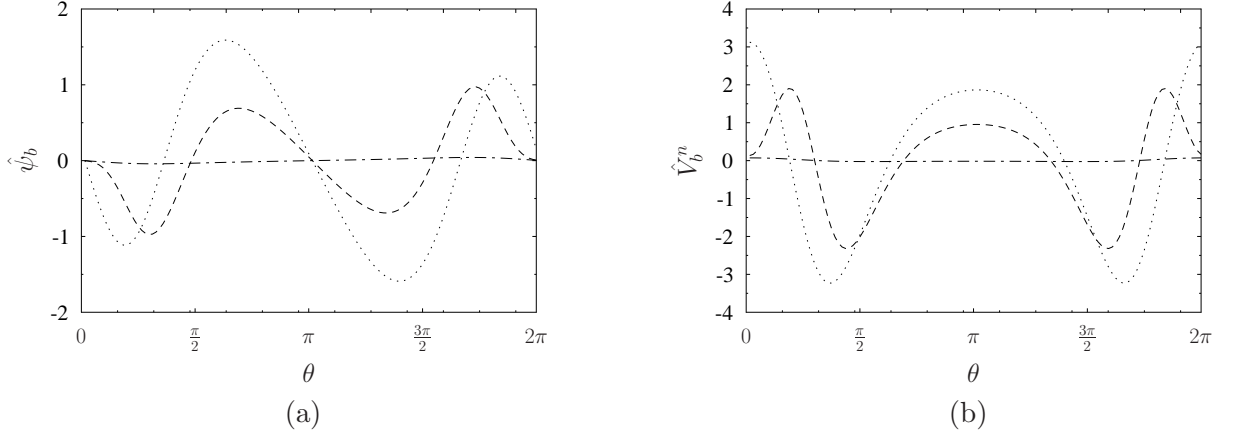


Fig. 9. (a) Optimal streamfunction boundary condition $\hat{\psi}_b$ and (b) the corresponding wall-normal velocity \hat{V}_b^n in (dashed line) case A, (dotted line) case B, and (dash-dotted line) case C.

- Case B: $\tilde{M}_1 = 62.500 + i27.245$,
- Case C: $\tilde{M}_1 = 54.836 + i37.671$.

Since for the vortex region $A(\psi_{b,0})$ corresponding to the zero boundary condition $\psi_{b,0} \equiv 0$ (Figure 5a) we have $M_1 = 55.725 + i27.478$, cases A and B correspond to shifting the vortex centroid from its original location towards, respectively, smaller and larger values of x . On the other hand, case C corresponds to shifting the centroid location towards larger values of y . In Figures 7a,b we present the decrease of cost functional $\mathcal{J}(\psi_b^{(k)})$ as a function of the iteration count k in the three cases. We note that while in cases A and B the cost functional is very rapidly reduced by more than 10 orders of magnitude, in case C the decrease is less significant and the iterations quickly saturate at a local minimum. This effect is further illustrated in Figure 8a where we show the paths traced in the complex plane by the moments M_1 during iterations in the three cases. We observe that while in cases A and B the moments M_1 rapidly approach \tilde{M}_1 , in case C the moments do not get close to the prescribed values of \tilde{M}_1 . This observation highlights the remark made in the previous paragraph, namely, that in some situations (viz. case C) there may be no solution of Euler system (4) corresponding exactly to the prescribed moment \tilde{M}_1 . We also remark that, interestingly, the paths in cases A and B do not approach the corresponding target values \tilde{M}_1 along straight lines, but rather along curved arcs, which reflect the topography of the control space in the two cases. Consistently with the results shown in Figures 7 and 8a, in Figure 8b we note significant shifts of the vortex region to the left in case A and to the right in case B with respect to the case with no control. On the other hand, in case C only a slight displacement of the vortex region can be observed. Next we show the optimal control $\hat{\psi}_b$ for the three cases in Figure 9a,

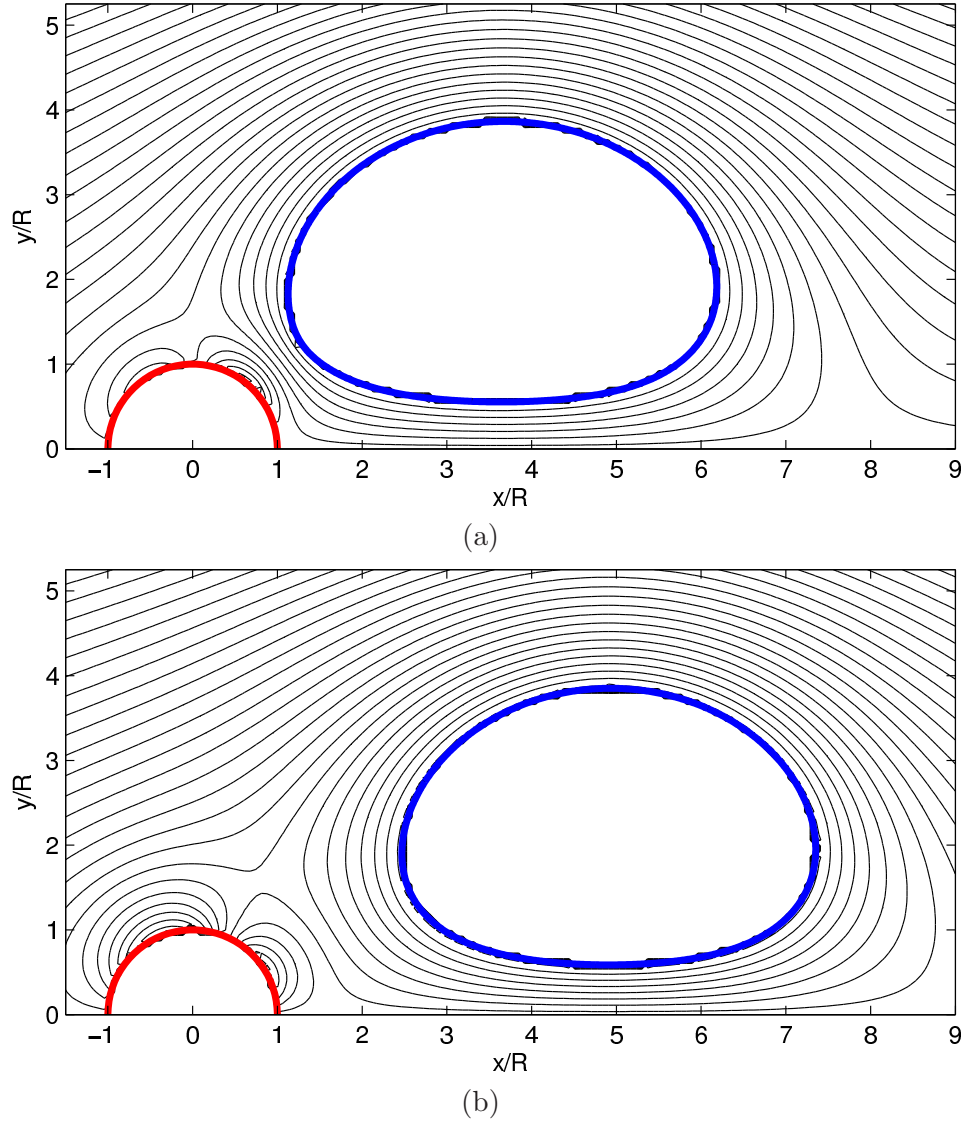


Fig. 10. The streamline patterns characterizing the optimal solution $\hat{\psi}$ in (a) case A and (b) case B; for clarity, streamlines are not plotted in the interior of the vortex region A.

and the corresponding wall-normal velocities \hat{V}_b^n in Figure 9b. We note that in cases A and B the blowing and suction velocity is quite significant reaching three times the level of the velocity of the unperturbed free stream at infinity in the latter case. On the other hand, in case C the blowing and suction velocity remains rather small, less than 10% of the velocity at infinity. Finally, in Figure 10 we present the streamline patterns in cases A and B (the streamline pattern for case C is not shown, since due to the small magnitude of the optimal control $\hat{\psi}_b$, it is quite similar to the streamline pattern shown in Figure 5a). Analyzing Figures 9b and 10a,b, we observe that the optimization algorithm arrives at two distinct control mechanisms in cases A and B. In case B the

vortex is pushed downstream by the control velocity forming a strong jet along the flow centerline. On the other hand, in case A the wall transpiration is deflected away from the flow centerline. Interestingly, in both cases A and B we note the presence of streamlines which issue from the front part of the obstacle and re-enter into the rear obstacle boundary after circumventing the vortex region. Further insights about the physics of the control mechanisms can be obtained from the pressure distributions shown in Figure 16 (for the ease of comparison, pressure plots corresponding to all cases are collected in one figure at the end of this Section). As compared to the flow without control (Figure 16a), in case A (Figure 16b) the pressure is significantly reduced in the region between the obstacle and the vortex, and this “suction zone” acts to attract the vortex towards the obstacle. On the contrary, in case B (Figure 16c) we note an extension of the high-pressure zone downstream which has the effect of moving the vortex further away from the obstacle.

We now move on to Step (ii) and consider two cases using the flows obtained in cases A and B of Step (i) as the points of departure. In each of these new cases the origin that the moments will be computed with respect to is shifted to the centroid of the vortex obtained in Step (i), i.e., to $z_0 = \frac{\tilde{M}_1}{|A|}$. As regards the first-order moments, we will therefore choose the new prescribed values as $\tilde{M}_1 = 0.0$. As regards the second-order moments, the following values are prescribed (for completeness, we also indicate the new values of z_0)

- Case AA: $\tilde{M}_2 = 25.0 + i0.0$, ($z_0 = 3.654 + i2.122$),
- Case BB: $\tilde{M}_2 = 0.0 + i0.0$ ($z_0 = 4.914 + i2.142$).

Since in each case the origin z_0 coincides now with the centroid of the vortex, the second-order moment M_2 admits a straightforward geometric interpretation. Writing the expression for this moment as

$$\begin{aligned} M_2 &= \int_A (z - z_0)^2 dA \\ &= \int_A [(x - x_0)^2 + (y - y_0)^2] dA + 2i \int_A (x - x_0)(y - y_0) dA, \end{aligned} \tag{43}$$

where $z_0 \triangleq x_0 + iy_0$, we note that the vanishing, large positive and large negative values of the real and imaginary parts of M_2 correspond to the vortex shapes indicated schematically in Figure 11. Thus, assuming the origin at z_0 , $\text{Re}(M_2)$ vanishes for regions A symmetric with respect to the line $y = \pm x$, whereas $\text{Im}(M_2)$ vanishes for regions A symmetric with respect to the axes $x = 0$ or $y = 0$. In regard to case AA, since the second-order moment characterizing the vortex region obtained at the end of Step (i) is $M_2 = 12.41 + i0.37$, this case corresponds to an attempt to elongate the vortex

region A in the horizontal direction. On the other hand, in regard to case BB, since the second-order moment characterizing the vortex region obtained at the end of Step (i) is $M_2 = 10.569 + i0.240$, this case represents an attempt to make the vortex region more circular. The choice of the weights in the two cases is $\alpha_1 = 10$, $\alpha_2 = 1$ which ensures that the vorticity centroids obtained in Step (i) will be approximately preserved during optimization of the second-order moments M_2 . In Figures 12a,b we show cost functionals $\mathcal{J}(\psi_b^{(k)})$ as a function of the iteration count k in cases AA and BB. We note a rather modest decrease in both cases suggesting that solutions of Euler equations (4) closely matching the prescribed moments \tilde{M}_2 may not in fact exist. This observation is further illustrated in Figures 13a,b,c where we show the paths traced by the moments M_1 and M_2 in the complex plane in the two cases. We remark that the moments M_2 move a little closer to their respective prescribed values \tilde{M}_2 , although this approach does not follow the shortest path. This also occurs at the cost of allowing for deviations of M_1 from zero, although in principle the extent of these deviations could be reduced by increasing the ratio of the weights $\frac{\alpha_1}{\alpha_2}$. Figure 13d shows the boundaries of the resulting vortex regions $A(\hat{\psi}_b)$ in the two cases. We emphasize that the actual shape modifications of these regions are consistent with the prescribed values of \tilde{M}_2 . In case AA the vortex region indeed becomes more elongated in the horizontal direction and features a gentle protuberance in its section nearest to the obstacle which corresponds to an increase of the imaginary part of M_2 , cf. Figures 11b and 13b. In case BB the vortex region becomes more circular. The optimal boundary distributions of the streamfunction $\hat{\psi}_b$ are shown in Figure 14a, whereas Figure 14b illustrates the corresponding wall-normal velocities \hat{V}_b^n in the two cases. It should be remarked that this transpiration velocity attains fairly large values in both cases, well over four times larger than the velocity of the unperturbed stream at infinity. The streamline patterns in cases AA and BB are shown, respectively, in Figures 15a and 15b. As compared to case A, in case AA we observe a strengthening of the transpiration velocity resulting in a further decrease of the pressure in the region between the obstacle and the vortex (Figure 16d), and the appearance of the aforementioned protuberance in the vortex boundary. In comparison to case B, in case BB we note that the transpiration velocity has an entirely different profile with an opposite phase (Figures 9b and 14b), so that the streamwise jet evident in case B is now replaced with a strong streamwise suction velocity. It is then intriguing to observe that two such vastly different forms of actuation give rise to flows with vortex regions with quite similar geometries (Figure 13d). However, the global streamline pattern in case BB is quite different from the flow pattern in case B (Figures 10b and 15b), as now most of the streamlines issuing from the obstacle boundary encircle the vortex region. The pressure distribution in case BB also features a high-pressure region reaching further downstream than in the flow without control (Figures 16a,e). In the present investigation we did not attempt to perform optimization of higher-order ($n > 2$) moments, hence

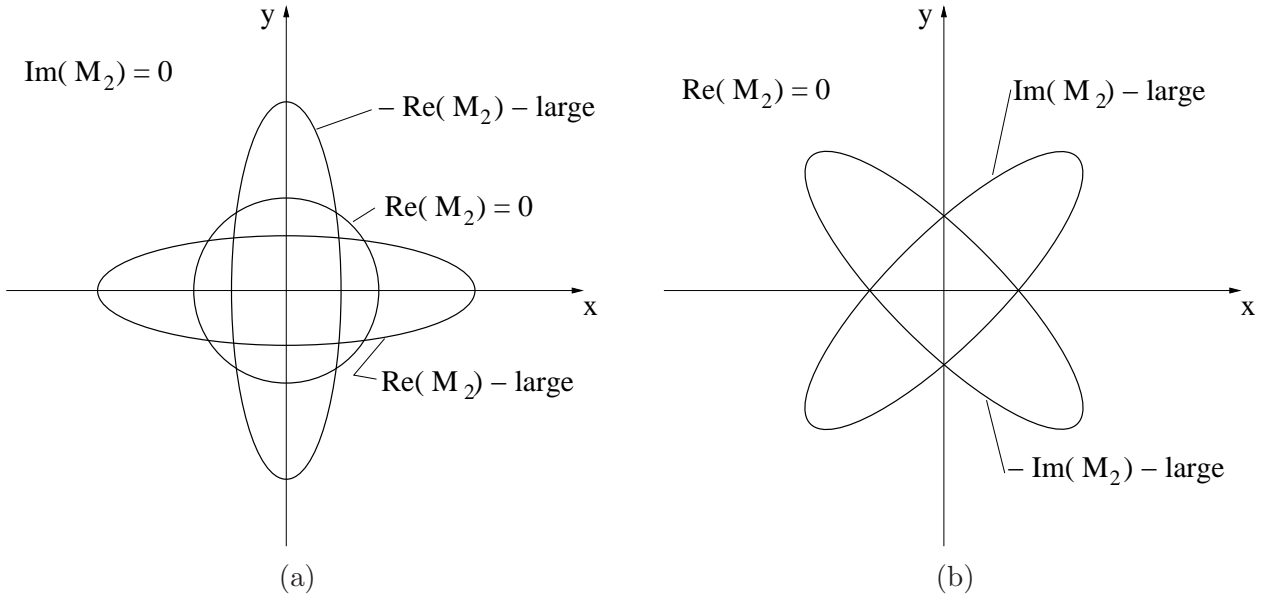


Fig. 11. Schematics illustrating the shapes of vortex regions characterized by (a) $\text{Im}(M_2) = 0$ and different values of $\text{Re}(M_2)$, and (b) $\text{Re}(M_2) = 0$ and different values of $\text{Im}(M_2)$. The origin is assumed at $z_0 = 0 + i0$, cf. (43).

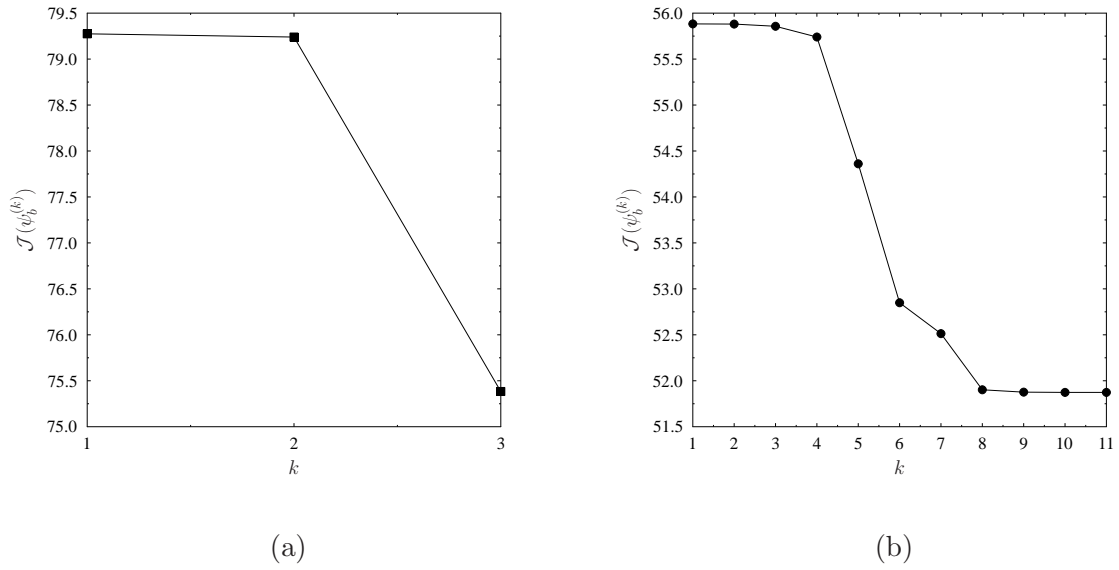


Fig. 12. Cost functional $\mathcal{J}(\psi_b^{(k)})$ as a function of the iteration count k in (a) case AA and (b) case BB.

this will conclude the presentation of our results.

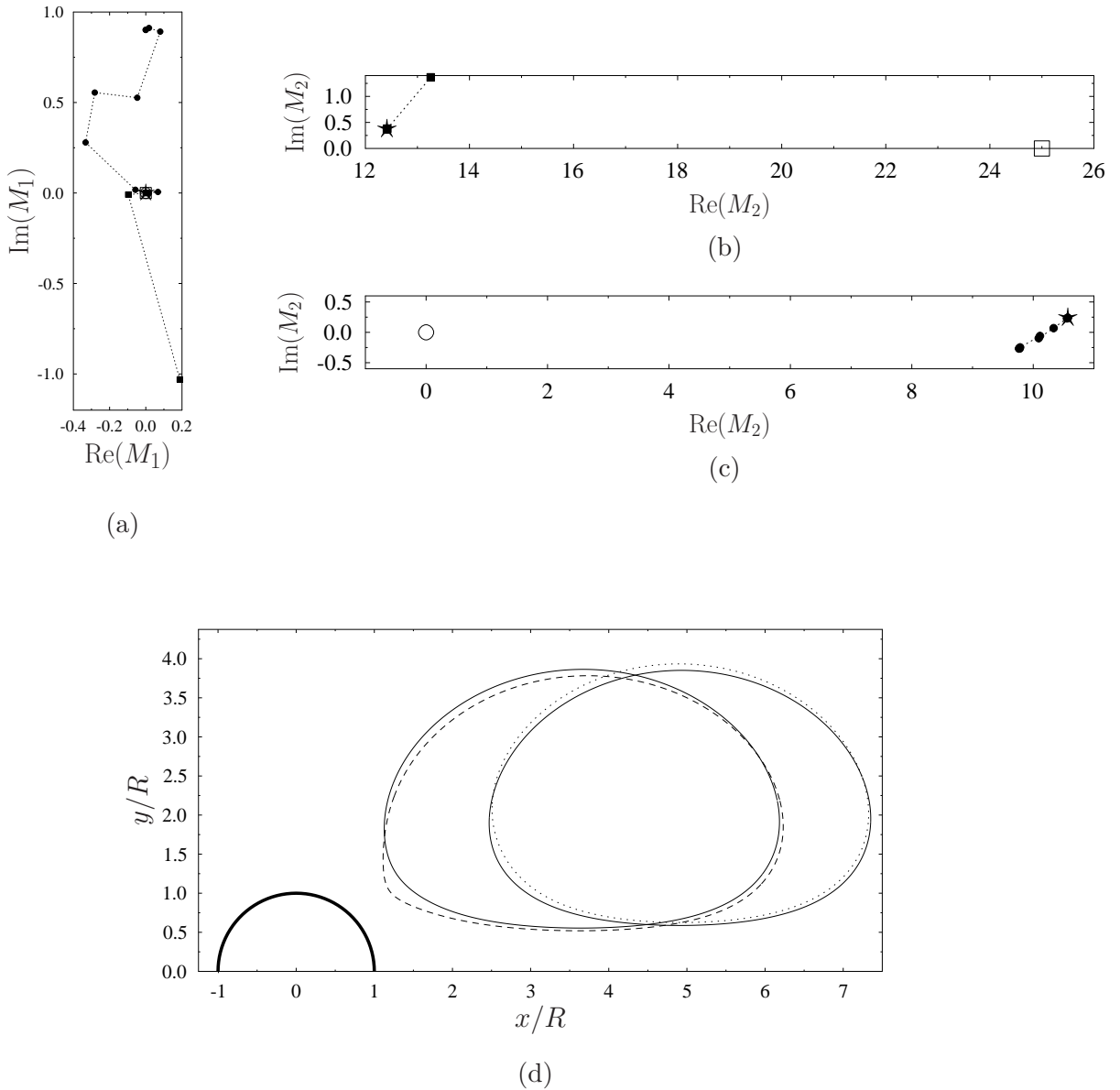


Fig. 13. Paths traced in the complex plane by the moments (a) M_1 and (b,c) M_2 during iterations for (squares) case AA and (circles) case BB; empty symbols represent the prescribed values \bar{M}_1 and \bar{M}_2 , and stars mark the values of M_1 and M_2 at the beginning of the iterations, (c) boundaries of the vortex region A in (solid lines) the flows obtained in Step (i), cases A and B, (dashed line) case AA and (dotted line) case BB; the thick solid line represents the obstacle boundary ∂B .

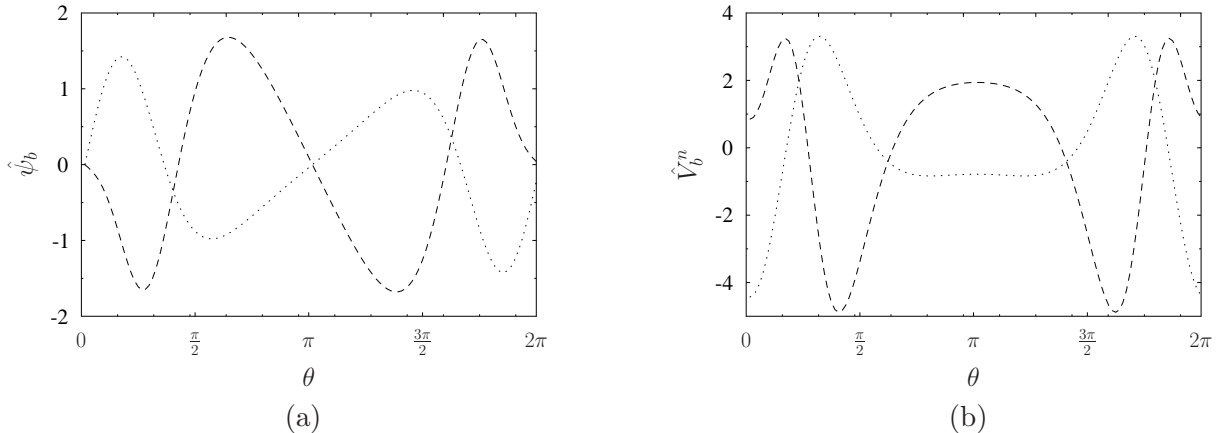


Fig. 14. (a) Optimal streamfunction boundary condition $\hat{\psi}_b$ and (b) the corresponding wall-normal velocity \hat{V}_b^n in (dashed line) case AA and (dotted line) case BB.

7 Discussion

Our computations for the test problem involving the Prandtl–Batchelor flow indicate that it is not always possible to “design” a vortex matching exactly all prescribed moments, even if the first-order and second-order moments are considered only. For the case with $N = 1$ (Step (i)), we were in fact able to identify control inputs such that the first-order moments were matched up to the machine precision in the cases corresponding to the streamwise (upstream and downstream) displacement of the vortices. On the other hand, we were unable to find a control input corresponding to a transverse displacement of the vortices indicating a limitation on the control authority of the investigated form of actuation. For the case with $N = 2$ (Step (ii)), although the prescribed values of the moment M_2 were not attained, with our approach we were able to achieve some desired modifications of the shape of the vortices. We conclude, therefore, that the prescribed moments $\tilde{M}_1, \dots, \tilde{M}_N$ should be regarded as indicating only the “direction” in which the corresponding property of the vortex region should change, rather than as the numerical values to be exactly matched. By comparing the data from Figures 9, 10, 14 and 15, we note that rather modest modifications of the location and shape of the vortex region A are in some cases accompanied by quite large changes of the optimal control $\hat{\psi}_b$, which is a signature of an ill-posed character of the vortex design problem. We stress, however, that such ill-posedness is a very common feature of most realistic inverse problems [53]. Although we did not find it necessary in the present problem, ill-posedness can be dealt with using various forms of regularization, e.g., with Tikhonov’s approach.

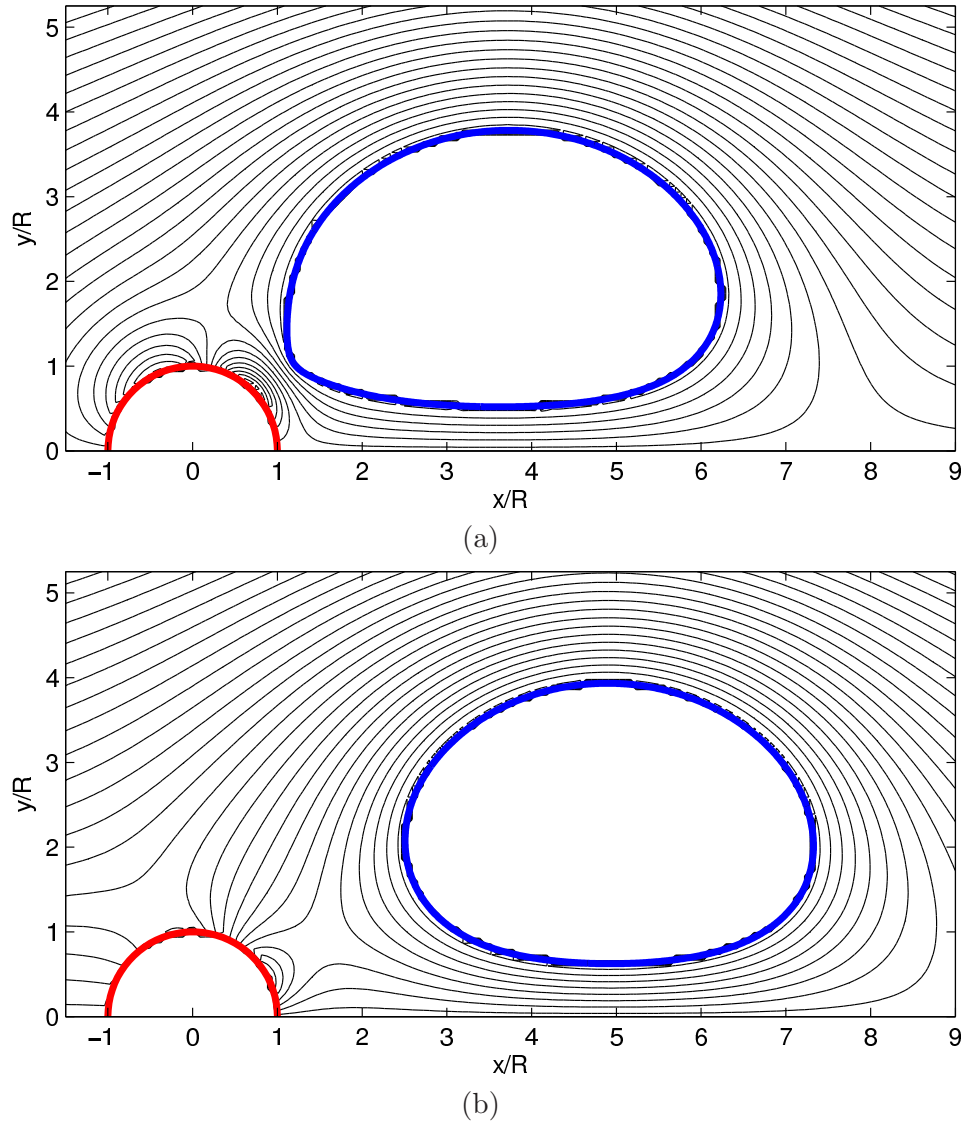


Fig. 15. The streamline patterns characterizing the optimal solution $\hat{\psi}$ in (a) case AA and (b) case BB; for clarity, streamlines are not plotted in the interior of the vortex region A .

Finally, we remark that our vortex design problem was formulated with the assumption $|A| = \text{const}$, cf. statement (8), however, in the actual computations reported in Section 6 the condition $|A| = \text{const}$ is not satisfied up to the machine precision. The reason is that during the solution of direct problem (4) this condition is quite difficult to enforce exactly — in practice, we ensure that the first variation (i.e., the shape differential) of this condition vanishes for contours constructed at every Newton iteration. Therefore, detected deviations from the condition $|A| = \text{const}$ result from the accumulation of higher-order errors. This is overall a small effect without any noticeable impact on the performance of our proposed approach.

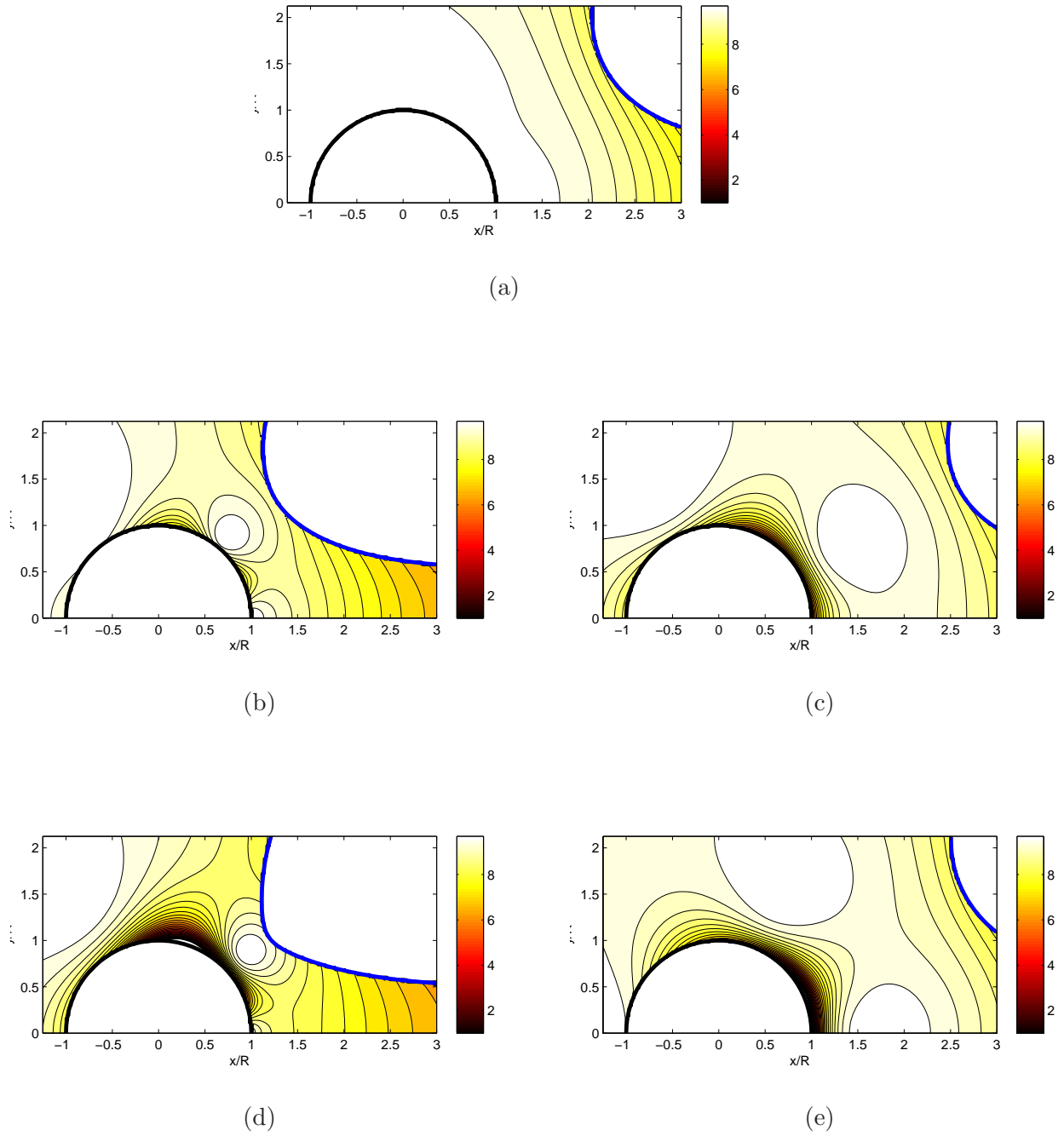


Fig. 16. Pressure distributions obtained in Euler flows representing (a) the reference case with $\psi_b \equiv 0$, (b) case A, (c) case B, (d) case AA, and (e) case BB. The value of the Bernoulli constant is arbitrarily chosen as $P_0 = 10$. For clarity, isolines and color-coding are omitted in regions corresponding to very low pressure [Figure (d)] and inside the vortex region A.

8 Conclusions

In this investigation we formulated and validated an adjoint-based approach to solution of optimal control problems for steady-state vortex systems with compactly supported vorticity. A distinguishing feature of this approach is that the internal interfaces (vortex boundaries) are tracked explicitly using methods of the shape differential calculus, in contrast to grid-based “interface-capturing” methods, such as the level-set techniques, which were recently proposed for similar problem [22]. In this sense, our method is close to the spirit of the “contour dynamics” approach typically employed to compute the evolution and steady states of such vortex flows. In fact, while in the present work the gradient information was obtained, via shape differentiation and adjoint analysis, from PDE system (4), entirely equivalent information could be obtained from the corresponding integral formulation of (4) given in terms of Green’s functions, thus making the connection with “contour dynamics” even more evident. We also stress that the main advantage of our adjoint-based approach is that one can obtain the gradient of the cost functional by solving a *single* linear problem which is significantly easier to solve than governing system (4).

It might appear as a plausible alternative to formulate the problem of vortex design in way that would make use of one of high-level optimization routines available in a computing environment such as MATLAB. However, such routines typically compute an approximation of the discrete gradient with some finite-difference formula. Aside from subtle issues related to the free-boundary nature of the present problem, to compute the discrete gradient such an approach would require at least one solution of system (4) for *every* discrete degree of freedom in the control variable [11]. Since this number of degrees of freedom tends to be significant, $\mathcal{O}(10^2)$ here, this approach would result in a prohibitive computational cost.

In addressing the simplest problem of optimal design of steady Euler flows with finite-area vortices we made a first step towards developing a framework for control and optimization of more complicated vortex flows with compact vorticity based on shape analysis. Indeed, generalization of the method proposed here to such more complex flows appears feasible. As regards flows featuring vortex sheets, the starting point is a free-boundary formulation analogous to (4), but with suitably modified interface conditions. It is possible that in problems involving vortex sheets the integral formulation (in terms of Green’s functions) might actually prove more tractable than the PDE formulation pursued here. An aspect of this problem which will require special attention is the treatment of the sheet endpoints. As regards generalization of the present method to time-dependent problems, it will involve the use the “noncylindrical calculus” [54] which

is an extension of the classical shape calculus to problems involving time. While technical details of this approach tend to be somewhat more involved than in the steady case, the general spirit of this approach is very similar. More specifically, in such formulations the optimality system will include an additional adjoint variable satisfying a PDE, the so-called “transverse equation”, defined on the interface (vortex boundary in the present problem). We have already successfully tested this approach on a simple model problem [55]. Both these generalizations, to include vortex sheets and address time-dependent problems, are subjects of ongoing research and results will be reported in the near future. We also mention that generalizations to three-dimensional problems are possible, as long as the system admits a free-boundary description in terms of “vortex dynamics”, such as in [56, 57]. Framing a vortex dynamics problem in terms of shape-differential formalism seems to be a novel approach and it was very recently also used in [31] to study the continuation of solutions of Euler system (4) with respect to parameters. In a related effort, shape-differentiation techniques emerge as a key ingredient of a novel approach to the investigation of stability of vortex patches which is currently being developed.

We also want to emphasize that inverse problems involving objectives other than the geometry of the vortices, e.g., optimization of the pressure distribution on the obstacle boundary or velocity in some parts of the flow domain, and formulated for Euler system (4) can also be treated in a straightforward manner using the proposed approach. One such problem of significant practical interest concerns optimization of lift on a wing with a trapped vortex, although due to limitations inherent in models based on the Euler equation and discussed in Section 2, the drag is always zero and cannot be optimized. Such extensions would still require the use of the same shape-differential formalism and would result in the adjoint system and the cost functional gradient with analogous structure (in fact, the only difference would be in how the adjoint system is forced, cf. (26d)).

Acknowledgements

The author wishes to thank Alan Elcrat for interesting discussions, and is also grateful to Professors Alan Elcrat and Ken Miller for providing him with the code for solution of Euler system (1)–(2) developed in [47]. Funding through a Discovery Grant from NSERC (Canada) is acknowledged.

References

- [1] M. A. Jones, “The separated flow of an inviscid fluid around a moving flat plate”, *J. Fluid Mech.*, **496**, 405–441, (2003).
- [2] T. Y. Hou, V. G. Stredie, and T. Y. Wu, “Mathematical modeling and simulation of aquatic and aerial animal locomotion”, *J. Comp. Phys.*, **225**, 1603–1631, (2007).
- [3] R. K. Shukla and J. D. Eldredge, “An inviscid model for vortex shedding from a deforming body”, *Theor. Comput. Fluid Dyn.* **21**, 343–368, (2007).
- [4] S. Alben, “Simulating the dynamics of flexible bodies and vortex sheets”, *J. Comp. Phys.*, **228**, 2587–2603, (2009).
- [5] S. Alben, “Regularizing a vortex sheet near a separation point”, *J. Comp. Phys.*, **229**, 5280–5298, (2009).
- [6] E. Kanso, “Swimming in an inviscid fluid”, *Theor. Comput. Fluid Dyn.*, **24**, 201–207, (2010).
- [7] A. Surana and D. Crowdy, “Vortex dynamics in complex domains on a spherical surface”, *J. Comp. Phys.*, **227**, 6058–6070, (2008).
- [8] D. G. Dritschel and R. K. Scott, “On the simulation of nearly inviscid two-dimensional turbulence”, *J. Comp. Phys.*, **228**, 2707–2711, (2009).
- [9] E. R. Johnson, A. K. Hinds and N. R. McDonald, “Steadily translating vortices near step topography”, *Phys. Fluids* **17**, 056601, (2005).
- [10] D. I. Pullin, “Contour Dynamics Methods”, *Annual Review of Fluid Mechanics*, **24**, 89–115, (1992).
- [11] M. D. Gunzburger, ”Perspectives in flow control and optimization”, SIAM, Philadelphia, (2003).
- [12] B. Mohammadi and O. Pironneau, *Applied Shape Optimization for Fluids*, Oxford University Press, (2009).
- [13] S. Zhou and Q. Li, “A variational level set method for the topology optimization of steady-state Navier-Stokes flow”, *J. Comp. Phys.*, **227**, 10178–10195, (2008).
- [14] V. Heuveline and F. Strauß, “Shape optimization towards stability in constrained

- hydrodynamic systems”, *J. Comp. Phys.*, **228**, 938–951, (2009).
- [15] D. N. Srinath and S. Mittal, “An adjoint method for shape optimization in unsteady viscous flows”, *J. Comp. Phys.*, **229**, 1994–2008, (2010).
- [16] W. Walker and M. J. Shelley, “Shape optimization of peristaltic pumping”, *J. Comp. Phys.*, **229**, 1260–1291, (2010).
- [17] M. Hinze and S. Ziegenbalg, “Optimal control of the free boundary in a two-phase Stefan problem”, *J. Comp. Phys.* **223**, 657–684 (2007).
- [18] O. Volkov and B. Protas, “An inverse model for a free-boundary problem with a contact line: steady case”, *J. Comp. Phys.* **228**, 4893–4910, (2009).
- [19] B. Protas, “Vortex Dynamics Models in Flow Control Problems”, *Nonlinearity* **21**, R203–R250, (2008).
- [20] J. Sokolowski and J.-P. Zolésio, “Introduction to shape optimization: shape sensitivity analysis”, Springer, (1992).
- [21] M. C. Delfour and J.-P. Zolésio, “Shape and Geometries — Analysis, Differential Calculus and Optimization”, SIAM, (2001).
- [22] F. Chantalat, Ch.-H. Bruneau, C. Galusinski and A. Iollo, “Level-set, penalization and Cartesian meshes: A paradigm for inverse problems and optimal design”, *J. Comp. Phys.* **228**, 6291–6315, (2009).
- [23] P. G. Saffman, *Vortex Dynamics*, Cambridge University Press, (1992).
- [24] A. J. Majda and A. L. Bertozzi, *Vorticity and Incompressible Flow*, Cambridge University Press, (2002).
- [25] J.-Z. Wu, H.-Y. Ma and M.-D. Zhou, “Vorticity and Vortex Dynamics”, Springer, (2006).
- [26] G. Batchelor, “Steady laminar flow with closed streamlines at large Reynolds number”, *J. Fluid Mech.* **1**, 177-190, (1957).
- [27] G. Batchelor, “A proposal concerning laminar wake behind bluff bodies at large Reynolds numbers”, *J. Fluid Mech.* **1**, 388-398, (1957).
- [28] R. T. Pierrehumbert, “A family of steady, translating vortex pairs with distributed

- vorticity”, *J. Fluid Mech.* **99**, 129–144, (1980).
- [29] A. Elcrat, B. Fornberg, M. Horn and K. Miller, “Some steady vortex flows past a circular cylinder”, *J. Fluid Mech.*, **409**, 13–27, (2000).
- [30] L. Föppl, “Wirbelbewegung hinter einem Kreiscylinder”, *Sitzb. d. k. Bayer. Akad. d. Wiss.* **1**, 1-17, (1913).
- [31] F. Gallizio, A. Iollo, B. Protas, and L. Zannetti, “On Continuation of Inviscid Vortex Patches”, *Physica D* **239**, 190–201, (2010).
- [32] B. Protas, “Linear Feedback Stabilization of Laminar Vortex Shedding Based on a Point Vortex Model”, *Physics of Fluids* **16**, 4473–4488, (2004).
- [33] S. Childress, *An Introduction to Theoretical Fluid Mechanics*, American Mathematical Society, (2009).
- [34] J. Cox, “The Revolutionary Kasper Wing”, *Soaring* **37** 20–23, (1973).
- [35] M.-K. Huang and Ch.-Y. Chow, “Trapping of a Free Vortex by Joukowski Airfoils”, *AIAA Paper* 82–4059, (1982).
- [36] The *VortexCell2050 project* funded by the European Commission within its FP6 Programme, contract number AST4–CT–2005–012139 (more information available at www.vortexcell2050.org).
- [37] L. M. Milne–Thompson, *Theoretical Hydrodynamics*, MacMillan, London (1955).
- [38] H. Salman and M. Soteriou, “Lagrangian simulation of evaporating droplet sprays”, *Phys. Fluids* **16** 4601–4622, (2004).
- [39] N. I. Akhiezer & M. G. Krein, *Some Questions in the Theory of Moments* (Transl. Math. Monographs Am. Math. Soc.) Vol. **2** (Providence, RI: American Mathematical Society), (1990).
- [40] B. Gustafsson, Ch. He, P. Milanfar & M. Putinar, M., “Reconstructing planar domains from their moments”, *Inverse Problems* **16**, 1053–1070, (2000).
- [41] J. Nocedal and S. Wright, “Numerical Optimization”, Springer, (2002).
- [42] D. Luenberger, “Optimization by Vector Space Methods”, John Wiley and Sons, (1969).

- [43] M. S. Berger, “Nonlinearity and Functional Analysis”, Academic Press, (1977).
- [44] J. Simon, “Differentiation with respect to domain in boundary value problems”, *Numer. Funct. Anal. and Optimiz.*, **2**, 649–687, (1980).
- [45] N. I. Muskhelishvili, *Singular Integral Equations. Boundary Problems of Function Theory and Their Application to Mathematical Physics*, Dover, (1992).
- [46] W. Hackbusch, “Integral Equations: Theory and Numerical Treatment”, Birkhäuser, (1995).
- [47] A. Elcrat, B. Fornberg B and K. Miller, “Stability of vortices in equilibrium with a cylinder”, *J. Fluid Mech.* **544**, 53–68, (2005).
- [48] L. N. Trefethen, *Spectral Methods in Matlab*, SIAM, (2000).
- [49] J. P. Boyd, *Chebyshev and Fourier Spectral Methods* (second edition), Dover, (2001).
- [50] R. Kreiss, *Linear Integral Equations*, Springer, (1999).
- [51] W. H. Press, B. P. Flanner, S. A. Teukolsky and W. T. Vetterling, *Numerical Recipes: the Art of Scientific Computations*, Cambridge University Press, (1986).
- [52] C. Homescu, I. M. Navon and Z. Li, “Suppression of vortex shedding for flow around a circular cylinder using optimal control”, *Int. J. Numer. Meth. Fluids* **38**, 43–69, (2002).
- [53] A. Tarantola, “Inverse Problem Theory and Methods for Model Parameter Estimation”, SIAM, (2005).
- [54] M. Moubachir and J.-P. Zolésio, “Moving Shape Analysis and Control — Applications to Fluid Structure Interactions”, Chapman & Hall, (2006).
- [55] B. Protas and W. Liao, “Adjoint–Based Optimization of PDEs in Moving Domains”, *J. Comp. Phys.* **227**, 2707–2723, (2008).
- [56] A. Elcrat, B. Fornberg, and K. Miller, “Some Steady Vortex Flows Past a Sphere”, *J. Fluid Mech.*, **433**, 315–328, (2001).
- [57] K. Shariff, A. Leonard and J. H. Ferziger, “A contour dynamics algorithm for axisymmetric flow” *J. Comp. Phys.* **227**, 9044–9062, (2008).